

Article

An Evaluation of Glycerol Acetalization with Benzaldehyde over a Ferromagnetic Heteropolyacid Catalyst

Rami Doukeh ¹, Maria Răpă ², Ecaterina Matei ², Doina Prodan ³, Romuald György ⁴, Ancuta Trifoi ^{2,*} and Ionut Banu ^{4,*}

¹ Faculty of Petroleum Refining and Petrochemistry, Petroleum-Gas University of Ploiești, 39 Bucharest Blvd., 100680 Ploiești, Romania; rami.doukeh@yahoo.com

² Faculty of Material Science and Engineering, University Politehnica of Bucharest, 313 Splaiul Independentei, 060042 Bucharest, Romania

³ “Raluca Ripan” Chemistry Research Institute, Department of Polymeric Composites, Babeș Bolyai University, 400347 Cluj-Napoca, Romania

⁴ Chemical and Biochemical Engineering Department, University Politehnica of Bucharest, 1 Polizu Str., 011061 Bucharest, Romania

* Correspondence: ancuta_trifoi@yahoo.com (A.T.); i_banu@chim.upb.ro (I.B.)

Abstract: Tungstophosphoric acid ($H_3PW_{12}O_{40}$) supported on silica-coated magnetite nanoparticles has been prepared and used as a heterogeneous acid catalyst ($Fe_3O_4@SiO_2@HPW$) in the condensation of benzaldehyde (B) with glycerol (Gly) for the production of cyclic acetals. Physicochemical techniques, including scanning electron microscopy (SEM), transmission electron microscopy (TEM), Fourier-transform infrared spectrometry (FTIR), X-ray diffraction (XRD), thermogravimetric analysis (TGA), and N_2 physisorption were used to characterize the prepared catalyst. The effect of glycerol/benzaldehyde molar ratio (1/1 to 1/1.2), temperature (80–120 °C), and catalyst amount (1–5%) on glycerol conversion and the selectivity in main reaction products: benzoic acid, 2-phenyl-1,3-dioxolan-4-yl)methanol, 2-Phenyl-1,3-dioxan-5-ol, 2-phenyl-1,3-dioxolane, and methyl 2-hydroxy-3-phenylpropanoate was studied to evaluate the catalytic activity of the prepared $Fe_3O_4@SiO_2@HPW$ catalyst. The optimization of these process parameters was conducted using Box–Behnken design (BBD). Using the BBD methodology, the optimal parameters (120 °C, 1:1.15 glycerol: benzaldehyde, 5% catalyst) were determined, for a glycerol conversion of and cyclic acetals yield of 85.95% and 78.36%, respectively. The catalyst also exhibits excellent activity for glycerol acetalization with other aromatic aldehydes such as cinnamaldehyde, p-methyl-benzaldehyde, p-hydroxy-benzaldehyde, and vanillin.

Keywords: glycerol acetals; benzaldehyde; tungstophosphoric acid; magnetic catalyst; Box–Behnken



Citation: Doukeh, R.; Răpă, M.; Matei, E.; Prodan, D.; György, R.; Trifoi, A.; Banu, I. An Evaluation of Glycerol Acetalization with Benzaldehyde over a Ferromagnetic Heteropolyacid Catalyst. *Catalysts* **2023**, *13*, 782. <https://doi.org/10.3390/catal13040782>

Academic Editors: Maria Luisa Di Gioia, Luisa Margarida Martins and Isidro M. Pastor

Received: 18 March 2023

Revised: 14 April 2023

Accepted: 19 April 2023

Published: 21 April 2023



Copyright: © 2023 by the authors. Licensee MDPI, Basel, Switzerland. This article is an open access article distributed under the terms and conditions of the Creative Commons Attribution (CC BY) license (<https://creativecommons.org/licenses/by/4.0/>).

1. Introduction

The valorization of glycerol produced by the biodiesel industry is important for environmental issues and biodiesel process economics. It is crucial for many industries where glycerol is used as an intermediate compound to obtain added-value products by biochemical, chemical, thermochemical, or catalytic routes. This mainly focuses on the dehydration of glycerol to acrolein (an important chemical intermediate in many industries) [1–3], polymerization of glycerol to polyglycerols (surfactants used in the food, detergents, and cosmetics industries) [4–7], esterification to acylated esters -glyceryl diacetate, glyceryl triacetate (oxygenated fuel additives) [8–10], hydrogenolysis of glycerol to propandiol (an important intermediate in the polymer industry) [11–13], condensation with carbonyl groups to acetals and ketals (antiknock additives in combustion engines, oxygenated fuel additive, surfactant, and flavoring agent) [14], carboxylation to glycerol carbonate (electrolyte and solvent in batteries) [15,16], and the steam reforming of glycerol to hydrogen (fuel) [17–19]. Among them, the condensation of glycerol with carbonyl compounds (ketones and aldehydes) is one of the common glycerol valorization routes

described in the literature because valuable cyclic acetals/ketals for various industries are obtained with the formation of H₂O as a non-toxic co-product. They are employed as scents or flavors in the food and cosmetic industries [20], additives for diesel fuel [21–25], green solvents [26,27], bases for surfactants [28], and many other applications with potential use in industry [29].

Traditionally, these reactions are performed in the presence of acidic homogenous catalysts [22], but because of their environmental issues (they cannot be recovered from the reaction system), various heterogeneous acid catalysts have been investigated. Acidic exchange resin [30,31], zeolites [32–35], carbon-based catalysts [36,37], transition or noble metals and metal oxides [38,39], functionalized mesoporous silica [40], heteropolyacids [41,42] or metal-organic frameworks [43,44] are promising versatile heterogeneous acid catalysts for cyclic acetal production from glycerol and aldehydes or ketones. Generally, the use of heterogeneous catalysts in industry and their efficiency has increased, but while in some cases the recovery of these catalysts is successful (usually by filtration), in other cases, it still remains challenging.

Catalysts supported on a magnetic material (i.e., magnetite) are an interesting alternative to heterogeneous catalysts. Due to their unique properties: non-toxic, low cost, environmentally friendly, and abundant, a wide variety of molecules of magnetite can be easily immobilized and supported on the catalyst surface. Furthermore, easy recovery by an applied magnetic field is a good choice for developing supported catalysts [45–48].

Tungstophosphoric acid (HPW) has enabled enormous progress in various acid-catalyzed reactions because of their structural mobility, super acidity, low volatility, low corrosivity, and high activity and selectivity for several reactions when compared to conventional mineral acids [49,50]. It has already been proven to be an efficient catalyst in acetalization reactions. Ferreira et al. [51] reported a study about the acetalization reaction between acetone and glycerol using heteropolyacids immobilized onto silica as catalysts. The highest catalytic activity was achieved by tungstophosphoric acid with more than 99% conversion of glycerol with 97% selectivity toward solketal (optimized conditions: glycerol to acetone = 1:6; temperature = 70 °C; catalyst loading = approximately 5 wt% wrt. Glycerol). The efficiency of the catalyst was attributed to the acidic strength of the catalyst, with an initial electrode potential $E_i = 290$ mV, determined by potentiometric titration with *n*-butylamine. The catalyst also showed good stability, demonstrated by consecutive runs. Good results for glycerol acetalization with formaldehyde over tungstophosphoric salts were also reported by Chen et al. [41,52]. A series of tungstophosphoric acid catalysts supported on metal oxides (TiO₂, CeO₂, ZrO₂) were designed to study the conversion of glycol and benzaldehyde to acetals in work by Li et al. [53]. Among them, 20 wt% H₃PW₁₂O₄₀/TiO₂ catalysts have demonstrated the highest activity, with more than 90% acetal yield. Recently, Castanheiro et al. [54] reported the use of tungstophosphoric acid encapsulated on a NaY zeolite in the acetalization of glycerol with an aromatic aldehyde (namely cinnamaldehyde), yielding a glycerol conversion of 89%, after 5 h of reaction at 100 °C and a molar ratio of glycerol:cinnamaldehyde of 1:2.25. Furthermore, the catalyst NaY-tungstophosphoric acid exhibited good catalytic stability.

A magnetite-based functionalized acid catalyst for acetal production using ethylene glycol and benzaldehyde was studied by Hosseini and Masteri Farahani [55]. They designed a catalyst with double acid type groups (sulfonic acid and phosphotungstic) that proved to be efficient in the reaction of benzaldehyde with ethylene glycol in the reaction condition: benzaldehyde to ethylene glycol molar ratio = 1/3, solvent: cyclohexane, 6.66 g cat/mol benzaldehyde at 90 °C. After 2 h of reaction, the benzaldehyde conversion reached 97%. Catalyst reuse studies were also performed, and the reported results indicated that the catalyst maintained its stability after at least four cycles of reaction. This paper presents important findings, but the studies are limited to fixed parameters without optimization of the process parameters.

Rajkumari and coworkers [56] studied the ultrasound-assisted synthesis of solketal using glycerol and acetone over a sulfonic acid-functionalized magnetic catalyst. After

synthesis and characterization of the catalyst, they also performed optimization studies on the reaction to improve the five-membered solketal ring yield, varying the catalyst amount, glycerol:acetone molar ratio, reaction time, agitation conditions, and temperature. They reached a high conversion of glycerol (97%) with 100% solketal selectivity, using ultrasound-assisted synthesis, at room temperature, in a relatively short reaction time (15 min) with a glycerol:acetone molar ratio of 1:5 and a catalyst amount of 5 wt% wt. Glycerol.

Given the versatility of heteropolyacids as catalysts, the unique properties of magnetite as potential catalyst support, as well as the importance of glycerol valorization, a goal of the present work is to evaluate the catalytic activity of tungstophosphoric acid immobilized on silica coated magnetite for the synthesis of aromatic glycerol acetals—an important class of fine chemicals derived from glycerol. The reactions were conducted using aromatic aldehydes; the parameters selected for the optimization of the process were: reaction temperature, reactant molar ratio, and catalyst amount. Another goal of this work is to optimize the process parameters of aromatic acetals synthesis over the prepared catalyst using the Box–Behnken experimental design.

2. Results and Discussions

2.1. Catalyst Characterization

The SEM images of Fe_3O_4 , $\text{Fe}_3\text{O}_4@\text{SiO}_2$, and $\text{Fe}_3\text{O}_4@\text{SiO}_2@\text{HPW}$ are shown in Figure 1a–c. The catalyst and support are composed of non-uniform crystals with an irregular surface and particles of various sizes, which are composed of fine particles that are strongly agglomerated (due to the attractive forces between the magnetic particles). The presence of W and P (from HPW) in the structure of the catalyst was confirmed by EDS analysis (Figure 2) and by energy dispersive X-ray spectroscopy (EDX) (Figure 3 and Table 1) obtained from SEM analysis of the catalyst.

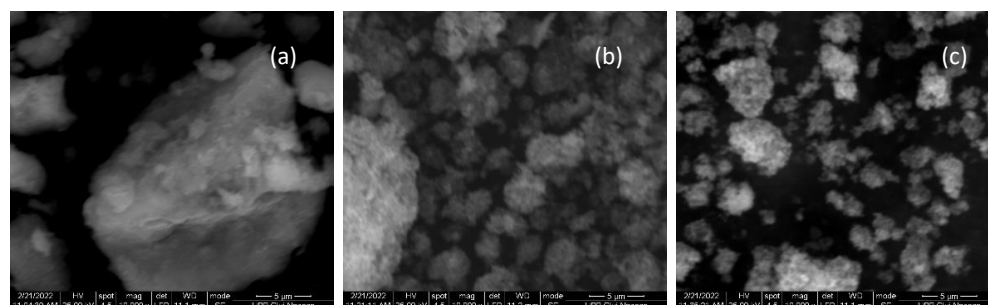


Figure 1. SEM microphotographs of (a) Fe_3O_4 , (b) $\text{Fe}_3\text{O}_4@\text{SiO}_2$, and (c) $\text{Fe}_3\text{O}_4@\text{SiO}_2@\text{HPW}$.

Table 1. EDS analysis of the $\text{Fe}_3\text{O}_4@\text{SiO}_2@\text{HPW}$ catalyst.

Element	Weight %	Atomic %
O K	59.90	77.81
SiK	22.16	16.39
P K	0.11	0.07
FeK	14.32	5.33
W L	3.51	0.40

Figure 4 shows the TEM images of the $\text{Fe}_3\text{O}_4@\text{SiO}_2@\text{HPW}$ catalyst. The sample is composed of a large number of congeries with a near-spherical shape. In addition, the TEM images confirm the formation of the core-shell structure of the catalyst. TEM images of the $\text{Fe}_3\text{O}_4@\text{SiO}_2@\text{HPW}$ catalyst showed that the size of the particles was less than 50 nm.

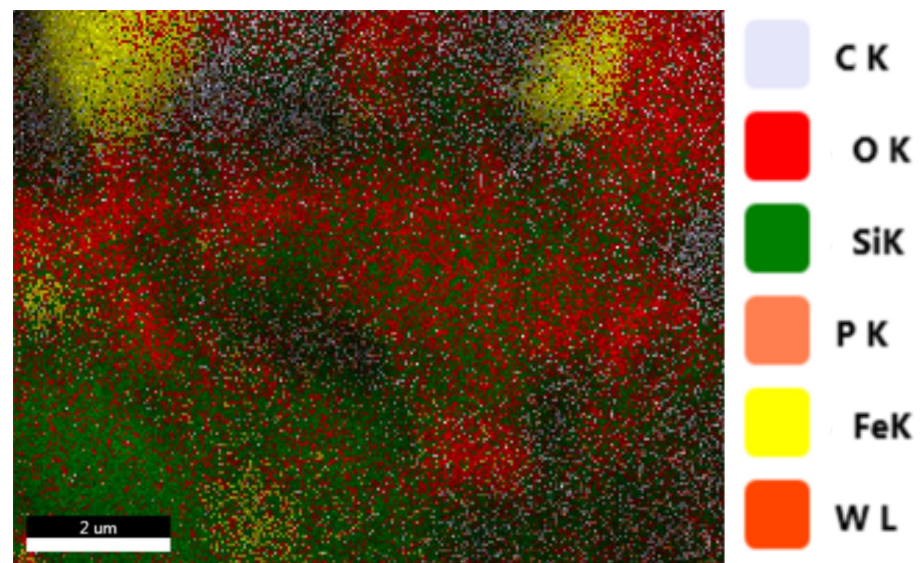


Figure 2. EDS element overlay map of the $\text{Fe}_3\text{O}_4@\text{SiO}_2@\text{HPW}$ catalyst.

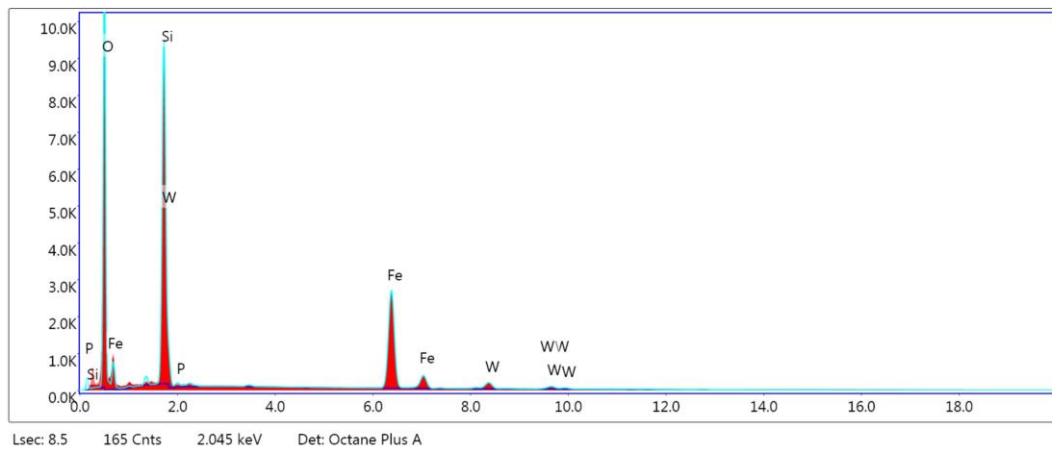


Figure 3. EDX spectrum of the $\text{Fe}_3\text{O}_4@\text{SiO}_2@\text{HPW}$ catalyst.

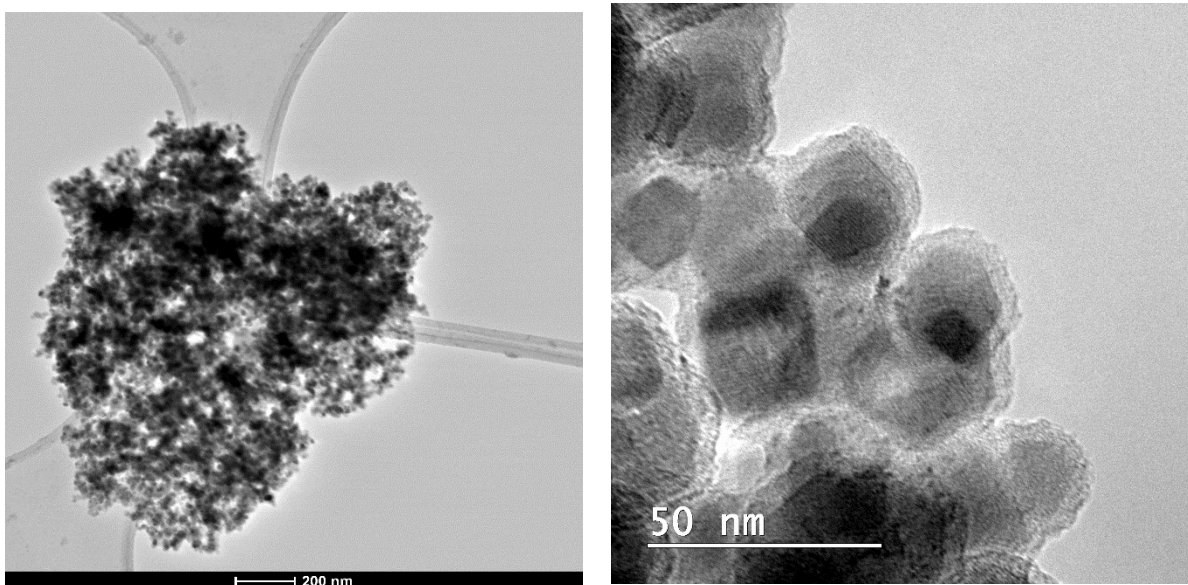


Figure 4. Transmission electron micrographs (TEM images) of the $\text{Fe}_3\text{O}_4@\text{SiO}_2@\text{HPW}$.

FTIR spectra of the synthesized materials are indicated in Figure 5. The FTIR spectrum of the synthesized Fe_3O_4 nanoparticles presents two peaks at 630 cm^{-1} and 590 cm^{-1} corresponding to the bonding of Fe-O [57,58] and two more bands in the wavenumber of 3400 cm^{-1} and 1630 cm^{-1} corresponding to the stretching and bending of H_2O molecules respectively [59]. The presence of a silica layer on the surface of magnetite is demonstrated in FTIR spectra by the vibration bands of Si-O bonds and silanol groups at wavenumbers 770 cm^{-1} and by the broad band at 1090 cm^{-1} [60–62]. The main FTIR bands of HPW are at about 1100 cm^{-1} (stretching frequency of P-O in the central PO_4 tetrahedron), 990 cm^{-1} (terminal bands for W=O in the exterior WO_6 octahedron), 890 cm^{-1} and 800 cm^{-1} (bands for the W-Ob-W and W-OcW bridge). In the FTIR spectrum of the $\text{Fe}_3\text{O}_4@\text{SiO}_2@\text{HPW}$ catalyst, some bands characteristic of the Keggin structure cannot be observed because they overlap with the bands of silica. All the bands that appeared in the FTIR spectra are in agreement with those reported in the literature [63–65].

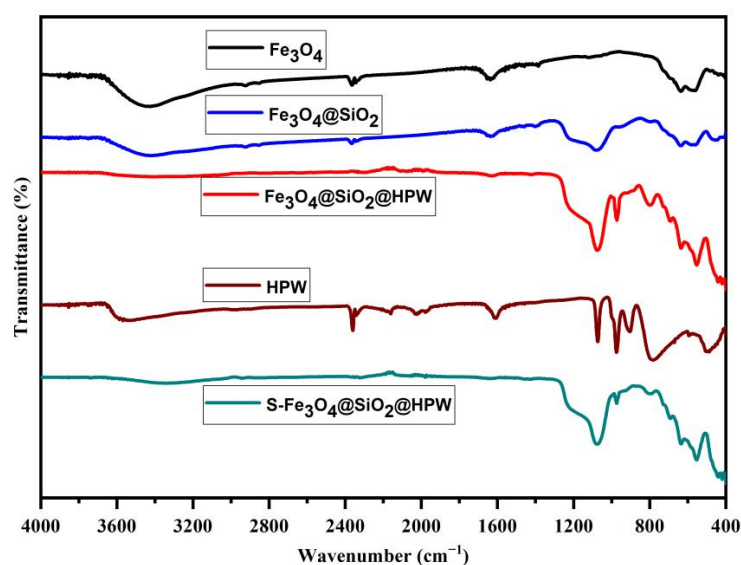


Figure 5. FTIR spectra of Fe_3O_4 , $\text{Fe}_3\text{O}_4@\text{SiO}_2$, $\text{Fe}_3\text{O}_4@\text{SiO}_2@\text{HPW}$, HPW, and spent catalyst (S- $\text{Fe}_3\text{O}_4@\text{SiO}_2@\text{HPW}$).

The $\text{Fe}_3\text{O}_4@\text{SiO}_2@\text{HPW}$ (fresh) and S- $\text{Fe}_3\text{O}_4@\text{SiO}_2@\text{HPW}$ (spent) FTIR spectra are similar; the characteristic bands of the heteropolyacid are still observed in the FTIR spectrum of the S- $\text{Fe}_3\text{O}_4@\text{SiO}_2@\text{HPW}$ catalyst, indicating that the Keggin structure of HPW is maintained after catalyst testing.

The Brønsted or Lewis nature of the acidic sites was determined by FTIR pyridine adsorption (Figure 6). The infrared spectra of pyridine at room temperature exhibits three absorption bands at 1580 , 1480 , and 1438 cm^{-1} . The Brønsted acid sites correspond to the 1580 cm^{-1} band (pyridinium ion), and the Lewis acid sites to the 1438 cm^{-1} band, attributed to coordinatively bounded pyridine [66]. The peak around 1480 cm^{-1} corresponds to the overlapping vibrations of pyridine adsorbed on both Lewis and Brønsted acid sites. Hence, the concentration of both the Brønsted and Lewis acid sites was calculated from their corresponding band intensities and extinction coefficients of each type of site using the equation reported by Isernia [67]. The results are presented in Table 2.

The XRD patterns of the catalyst and magnetic support were prepared in 2θ ranging from 10 to 80° (Figure 7a,b—magnified from 10 to 30°). The Fe_3O_4 sample exhibits the main peaks at $2\theta = 30.1$, 35.4 , 43.1 , 53.4 , 56.9 , 62.5 , and 74.9° characteristic for magnetite [68,69]. Similar peaks may be observed in the XRD diagrams of $\text{Fe}_3\text{O}_4@\text{SiO}_2$ support and $\text{Fe}_3\text{O}_4@\text{SiO}_2@\text{HPW}$ catalyst, confirming that the cubic phase of magnetite is kept after silica coverage and HPW molecule immobilization. The silica layer did not change the structure of Fe_3O_4 , except for the presence of a broad weak peak at 2θ range between 20° and 25° , indicating the presence of amorphous silica in the structure of the $\text{Fe}_3\text{O}_4@\text{SiO}_2$ and $\text{Fe}_3\text{O}_4@\text{SiO}_2@\text{HPW}$ samples [70–72] (Figure 7b). The

pattern for the $\text{Fe}_3\text{O}_4@SiO_2@HPW$ catalyst exhibits supplementary broad signals, characteristic to the lines of HPW structure at around $2\theta = 15.1^\circ, 18.3^\circ, 21.5^\circ, 23.2^\circ, 26^\circ,$ and 28° (Figure 7b), in agreement with published data [73–75].

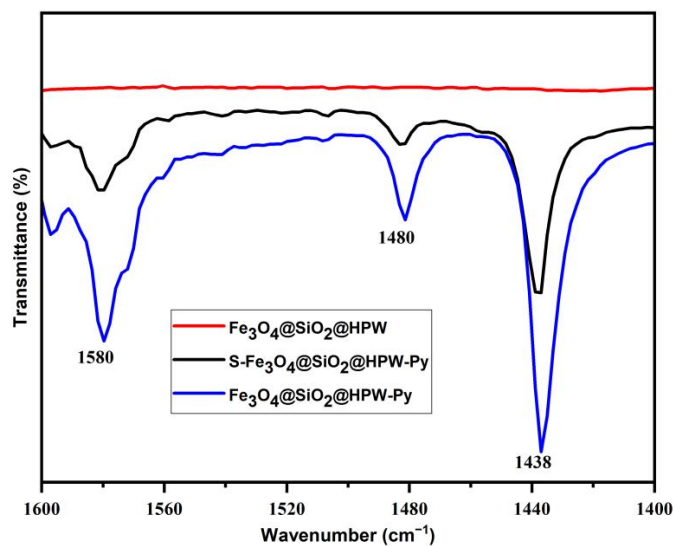
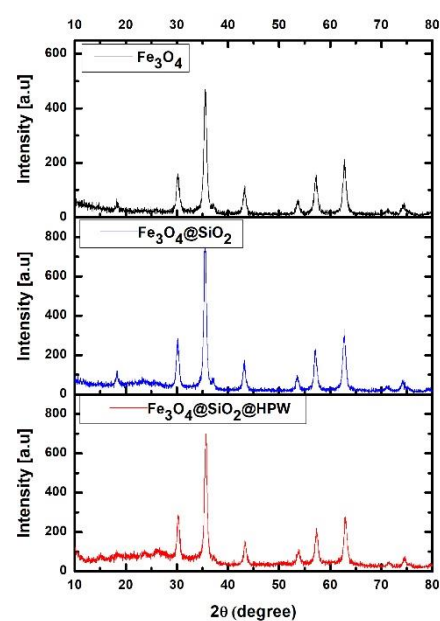


Figure 6. FTIR spectra of the catalyst with and without pyridine.

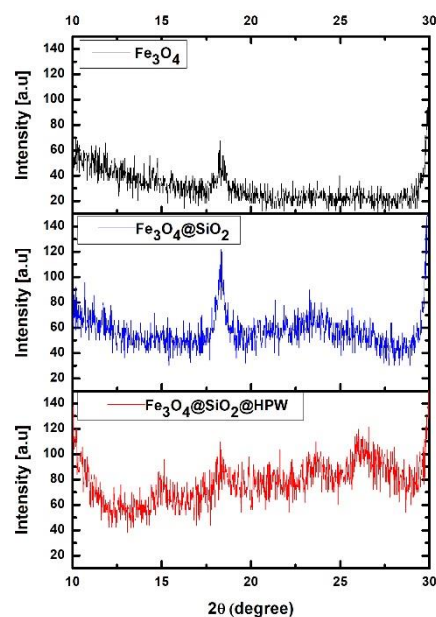
Table 2. The concentration of acidic sites.

Catalyst	$C_{\text{Lewis}} (C_L)$ mmol/g	$C_{\text{Lewis}} (%)$	$C_{\text{Bronsted}} (C_B)$ mmol/g	$C_{\text{Bronsted}} (%)$	Total Concentration	C_L/C_B Ratio
					$(C_L + C_B)$ mmol/g	
$\text{Fe}_3\text{O}_4@SiO_2@HPW$	39.92	63.08	23.36	36.92	63.28	1.7
$S\text{-Fe}_3\text{O}_4@SiO_2@HPW$	38.35	67.57	18.41	32.43	56.76	2.08



(a)

Figure 7. Cont.



(b)

Figure 7. XRD patterns of Fe_3O_4 , $\text{Fe}_3\text{O}_4@ \text{SiO}_2$, and $\text{Fe}_3\text{O}_4@ \text{SiO}_2@ \text{HPW}$ (a) $2\theta = 10\text{--}80^\circ$; (b) $2\theta = 10\text{--}30^\circ$.

Figure 8 displays the N_2 adsorption-desorption isotherms for the Fe_3O_4 , $\text{Fe}_3\text{O}_4@ \text{SiO}_2$, and $\text{Fe}_3\text{O}_4@ \text{SiO}_2@ \text{HPW}$ catalysts. In the silica-coated magnetite samples, $\text{Fe}_3\text{O}_4@ \text{SiO}_2$ and $\text{Fe}_3\text{O}_4@ \text{SiO}_2@ \text{HPW}$, the nitrogen adsorption-desorption isotherms present type IV isotherms with an H_3 hysteresis for materials with crack-type pores or flat particles (aggregates), according to the International Union of Pure and Applied Chemistry (IUPAC) classification [76]. Fe_3O_4 presents an H_1 hysteresis type, which is indicative of a material with cylindrical and uniform pores.

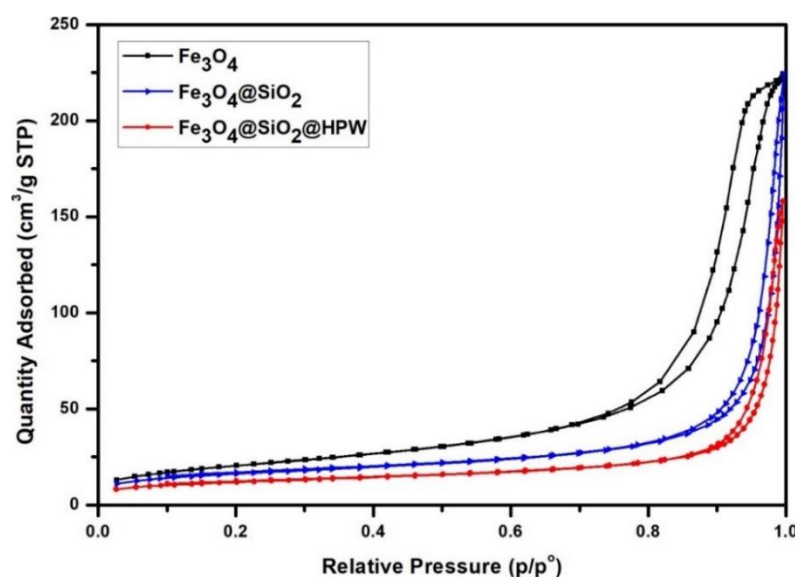


Figure 8. N_2 adsorption-desorption isotherms of Fe_3O_4 , $\text{Fe}_3\text{O}_4@ \text{SiO}_2$, and $\text{Fe}_3\text{O}_4@ \text{SiO}_2@ \text{HPW}$.

From the BJH pore-size distribution (Figure 9), multimodal type of pores as meso- (35 nm) and macro-pores (80–125 nm) are present in the $\text{Fe}_3\text{O}_4@ \text{SiO}_2$ and $\text{Fe}_3\text{O}_4@ \text{SiO}_2@ \text{HPW}$ samples. The bare Fe_3O_4 exhibits uniform pore size distribution with the unimodal mesoporous structure (10–40 nm mesopores).

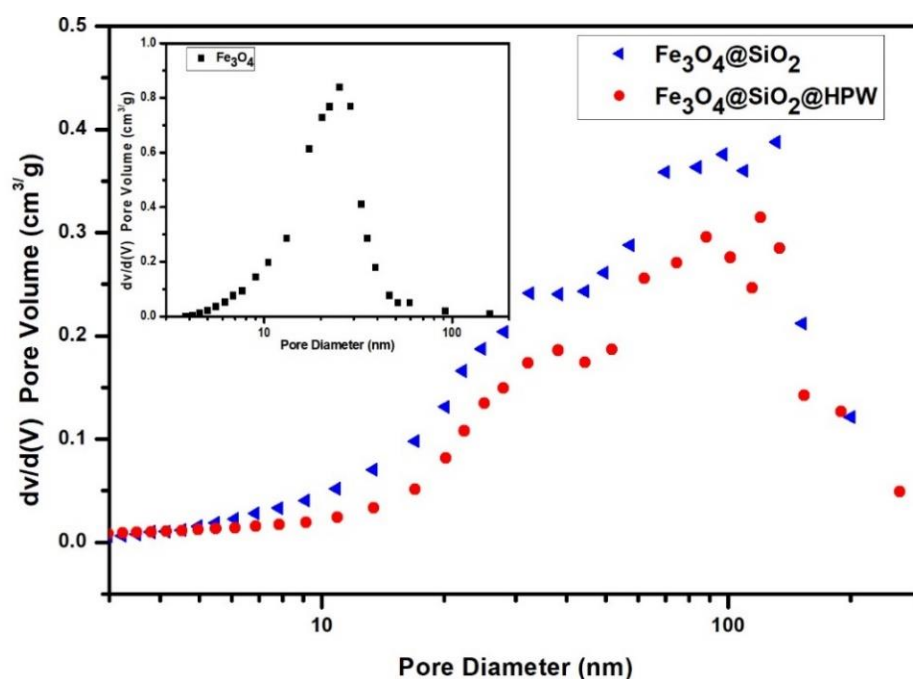


Figure 9. The pore size distribution of Fe_3O_4 , $\text{Fe}_3\text{O}_4@ \text{SiO}_2$, and $\text{Fe}_3\text{O}_4@ \text{SiO}_2@ \text{HPW}$.

Table 3 presents the values of the parameters that define the textural properties of the catalyst, namely the BET-specific area, the meso- and macro-pore volume, and the mean diameter. In the $\text{Fe}_3\text{O}_4@ \text{SiO}_2@ \text{HPW}$ catalyst, the BET surface area ($40.86 \text{ m}^2/\text{g}$) and pore volume ($0.24 \text{ cm}^3/\text{g}$) were decreased due to immobilization HPW molecules and structural rearrangement after catalyst calcination through $-\text{OH}$ group elimination.

Table 3. Textural characteristics of the bare Fe_3O_4 , $\text{Fe}_3\text{O}_4@ \text{SiO}_2$ support, and $\text{Fe}_3\text{O}_4@ \text{SiO}_2@ \text{HPW}$ catalyst.

Sample	Specific Area (BET) m^2/g	Pore Volume 2–300 nm (BJH Desorption) cm^3/g	Mean Diameter 2–300 nm (BJH Desorption) nm
Fe_3O_4	73.84	0.36	17.21
$\text{Fe}_3\text{O}_4@ \text{SiO}_2$	56.09	0.32	34.82
$\text{Fe}_3\text{O}_4@ \text{SiO}_2@ \text{HPW}$	40.86	0.24	36.4

The thermal stability of the catalyst was evaluated using thermogravimetric analysis to determine whether the Keggin structure of the active phase of the catalyst was preserved after testing. The TGA profile shown in Figure 10, corresponding to the unsupported HPW, indicates that the main weight loss (approx. 6.3%) occurred until $200 \text{ }^\circ\text{C}$. The DTG (derivative thermogravimetry) curve revealed four peaks of weight loss. In the first stage corresponding to peaks at $76 \text{ }^\circ\text{C}$ and $145 \text{ }^\circ\text{C}$, the loss of physically absorbed water is observed. At $195 \text{ }^\circ\text{C}$, crystallization water loss is observed, and in the last stage, corresponding to a peak of $540 \text{ }^\circ\text{C}$, the Keggin structure starts decomposing.

The TGA profile corresponding to the fresh $\text{Fe}_3\text{O}_4@ \text{SiO}_2@ \text{HPW}$ catalyst and spent S- $\text{Fe}_3\text{O}_4@ \text{SiO}_2@ \text{HPW}$ catalyst, presented in Figure 11, exhibits similar behavior, with the difference that the DTG curve of the spent catalyst revealed a higher mass loss in the stage corresponding to water loss, thus demonstrating that the catalyst structure is still preserved after testing.

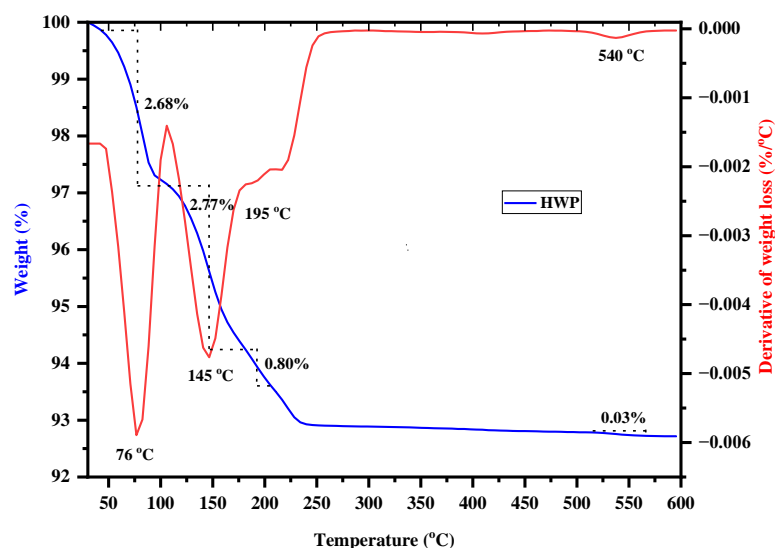


Figure 10. Thermogravimetric analysis (TGA) and derivative thermogravimetry (DTG) analysis of HPW.

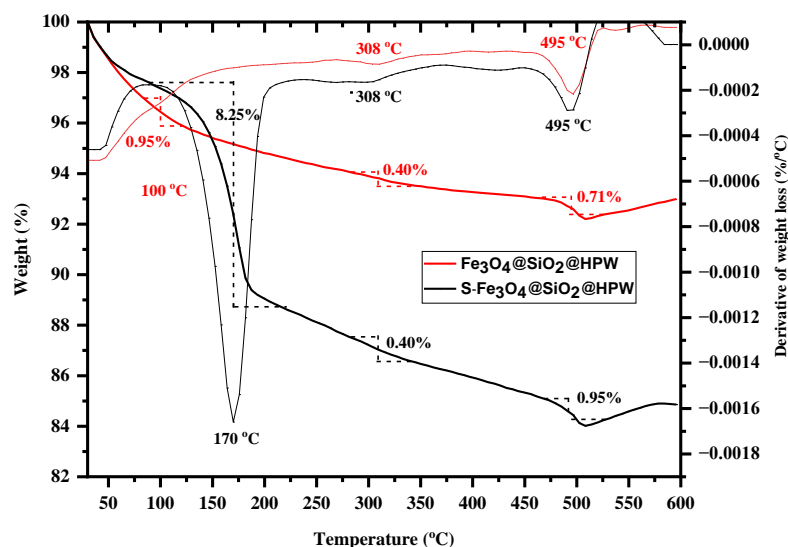


Figure 11. Thermogravimetric analysis (TGA) and derivative thermogravimetry (DTG) analysis of fresh $\text{Fe}_3\text{O}_4@ \text{SiO}_2@ \text{HPW}$ and spent $\text{S-Fe}_3\text{O}_4@ \text{SiO}_2@ \text{HPW}$ catalyst.

2.2. Effect of Process Variables

Instead of using the OFAT (one-factor at a time) approach, the influence of process variables was studied using a Box–Behnken experimental design. The desired major products in glycerol acetalization with benzaldehyde are the cyclic six-membered atoms (cis/trans-2-phenyl-1,3-dioxan-5-ol) and cyclic five-membered atoms (2-phenyl-1,3-dioxolan-4-yl) methanol and 2-phenyl-1,3-dioxolane). Moreover, the formation of non-cyclic acetal (methyl-3-hydroxy-3-phenylpropanoate), benzoic acid, and other minor products may also be observed (Figure 12). Yamamoto and co-workers [72] presented the reaction mechanism between benzaldehyde and glycerol and evidenced this possible reaction pathway with the formation of 2-phenyl-1,3-dioxolane-4-methanol which, in the presence of water and benzaldehyde, could form 2-phenyl-1,3-dioxolane as well as benzoic acid and methanol [72].

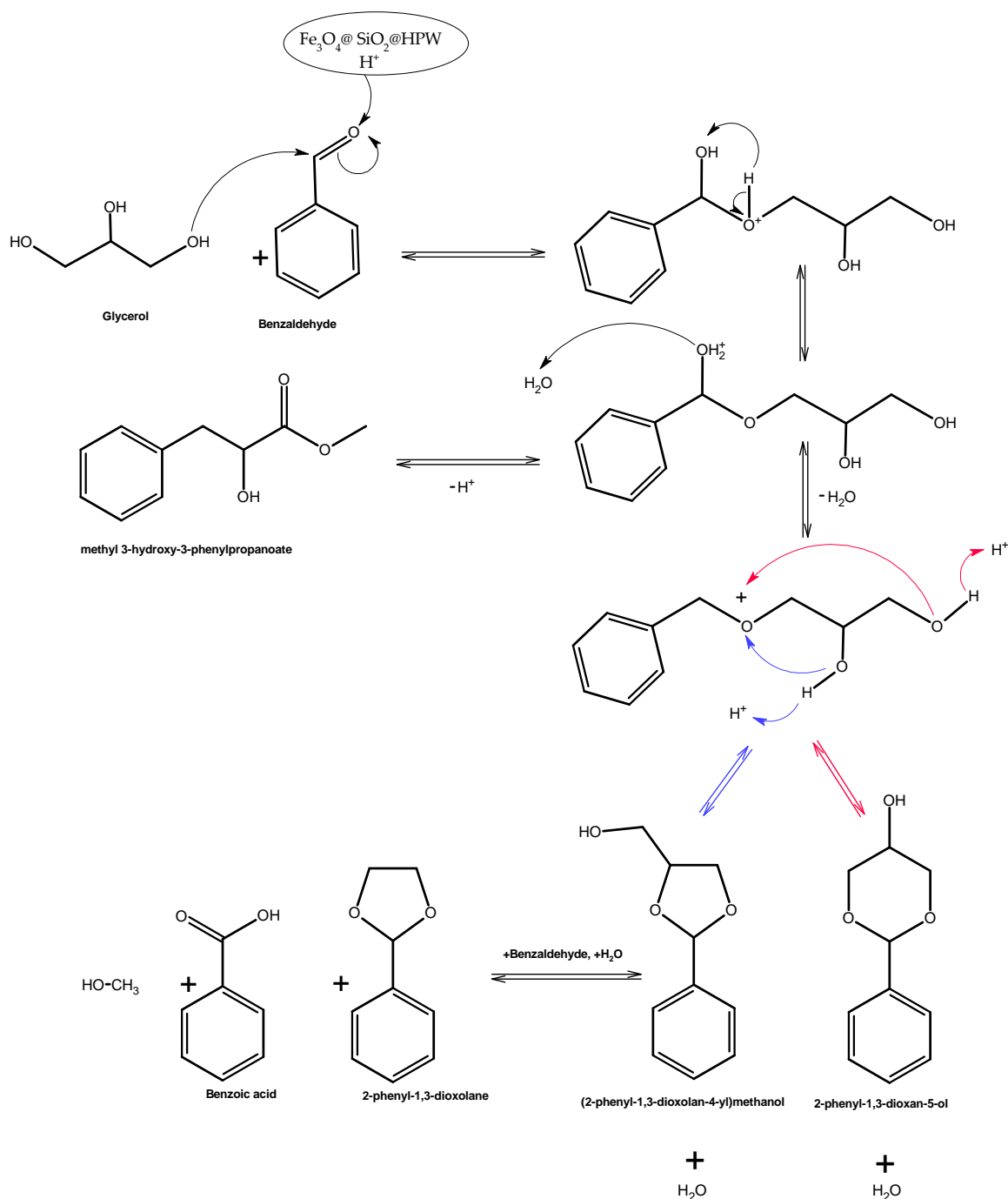


Figure 12. Reaction mechanism of acetalization of glycerol with benzaldehyde (based on the mechanism presented by Yamamoto et al. [77]).

A similar mechanism was proposed by Castanheiro [78] for the acetalization of glycerol with citral over a heteropolyacid immobilized on KIT-6. According to this study, it may be initiated by an interaction between an oxygen atom of a carbonyl group and Bronsted acid sites. Therefore, the formation of a hemiacetal in the reaction of benzaldehyde with glycerol may be followed by eliminating a water molecule and forming a carbocation. The latter suffers an attack involving the inner or terminal hydroxyl group of a glycerol molecule to ensure the formation of cyclic acetals. A similar mechanism was evidenced by Patel and Pithadia [79].

In our study, the presence of these chemical compounds in the chemical mixture was proven by GC-MS analyses (see Supplementary Information).

The determination of proper operating conditions is essential when dealing with condensation reactions. In the current case, the goal is to improve the yields in the cyclic acetals. At low temperature (80 °C) and a catalyst amount of 3%, the increase in the initial B/Gly mole ratio has a small effect both on glycerol conversion (61.11% at B/Gly = 1 vs. 60.41% at B/Gly = 1.2) and on yields in cyclic acetals (see experiments 5 and 12 in Table 4). By increasing the temperature to 120 °C for a catalyst amount of 3%, an increase of B/Gly from 1 to 1.2 has a larger influence on process performance in terms of 6-member acetal (an increase from 27.34% to 31.64%) and 5-member acetal (an increase from 24.97% to 29.58%). The increase in the B/Gly ratio at high temperatures also reduces the selectivity in secondary products (benzoic acid and non-cyclic acetal) (see experiments 1 and 4 in Table 4). This behavior was also emphasized by Kulkarni and Arvind [80] over a sulfated ceria-zirconia catalyst.

Table 4. Box–Behnken design matrix.

Experiment	X ₁	X ₂	X ₃	Y ₁	Y ₂	Y ₃	Y ₄	Y ₅	Y ₆
1	1	0	−1	1.49	16.54	27.37	24.97	8.13	78.51
2	0	−1	1	2.25	23.5	15.27	14.73	11.97	67.72
3	0	1	−1	2.89	27.38	17.18	17.58	15.13	80.16
4	1	0	1	1.04	11.78	31.64	29.58	6.27	80.31
5	−1	0	1	2.64	12.44	20.03	19.01	6.3	60.41
6	0	−1	−1	2.94	21.62	15.75	15.59	11.56	67.46
7	0	0	0	2.81	25.39	16.85	20.01	12.05	77.11
8	0	0	0	3	24.44	18.42	18.23	13.13	77.22
9	0	0	0	3.1	25.02	18.07	18.04	13.67	77.91
10	−1	−1	0	2.83	9.05	20.59	19.01	4.69	56.18
11	−1	1	0	2.8	14.41	17.71	18.22	8.53	64.67
12	−1	0	−1	3.45	10.66	20.84	20.31	5.84	61.11
13	0	1	1	2.63	28.22	16.72	17.03	15.84	80.44
14	1	1	0	1.06	13.2	33.81	31.72	7.25	87.05
15	1	−1	0	1.21	15.69	26.28	24.12	7.68	75.5

At 120 °C and a B/Gly ratio of 1.1, the increase of the catalyst amount in the mixture is leading, as expected, to a higher glycerol conversion and an increased selectivity in the cyclic acetals (for the 6-member one, from 26.28% to 33.81% whereas for the 5-member one from 24.12% to 31.72%) (see experiments 14 and 15 in Table 4).

The temperature increase has, as expected, an important effect on the increase of glycerol conversion, leading to a decrease in by-product selectivity and an increase in 5-member and 6-member acetals (see pair of experiments 4–5 and 11–14 in Table 4). This is explained by the increase of reaction rates with temperatures towards the formation of cyclic acetals.

2.3. Modeling of Process Performance

In order to evaluate the influences of the main factors on glycerol conversion and selectivity in acetals, a polynomial regression model expressed by Relation (1) was implemented, and its accuracy was evaluated using the analysis of variance techniques.

$$y = \beta_0 + \sum_{i=1}^k \beta_i X_i + \sum_{i=1}^k \beta_{ii} X_i^2 + \sum_{i=1}^{k-1} \sum_{j=2}^k \beta_{ij} X_i X_j + \varepsilon \quad (1)$$

The adequacy of the model was assessed by comparing the calculated Fisher test value (F-value) with the theoretical one (Ft(p-1, n-p)) for a chosen risk of 5% for a number of experiments of n and p terms in the model [81]. As mentioned in the literature regarding the statistical analysis, the parameter p-value parameter should be below 5% to consider the fact that each of the independent variables in the model is useful in predicting the system's response [82]. The coefficients of the models as well as statistical tests were evaluated using Design-Expert Version 8.0.7.1.

For each response, the analysis of variance data calculated based on the Box–Behnken design matrix is presented in Table 5. The estimated coefficients for each selectivity (Y_1 to Y_5) as well as for glycerol conversion (Y_6), together with their corresponding confidence intervals, are given in Relations (2)–(7).

$$Y_1 = 2.94(1 \pm 0.054) - 0.865(1 \pm 0.133) \cdot X_1 + 0.0188(1 \pm 6.132) \cdot X_2 - 0.2763(1 \pm 0.417) \cdot X_3 - 0.754(1 \pm 0.224) \cdot X_1^2 - 0.2319(1 \pm 0.729) \cdot X_2^2 \quad (2)$$

$$Y_2 = 25.08(1 \pm 0.043) + 1.33(1 \pm 0.757) \cdot X_1 + 1.67(1 \pm 0.604) \cdot X_2 - 0.0325(1 \pm 31) \cdot X_3 - 1.96(1 \pm 0.729) \cdot X_1 \cdot X_2 - 1.64(1 \pm 0.865) \cdot X_1 \cdot X_3 - 12.11(1 \pm 0.122) \cdot X_1^2 \quad (3)$$

$$Y_3 = 16.89(1 \pm 0.058) + 4.99(1 \pm 0.184) \cdot X_1 + 0.941(1 \pm 0.979) \cdot X_2 + 0.315(1 \pm 2.92) \cdot X_3 + 2.6(1 \pm 0.5) \cdot X_1 \cdot X_2 + 1.27(1 \pm 1.02) \cdot X_1 \cdot X_3 + 7.89(1 \pm 0.171) \cdot X_1^2 \quad (4)$$

$$Y_4 = 17.32(1 \pm 0.081) + 4.23(1 \pm 0.309) \cdot X_1 + 1.39(1 \pm 0.943) \cdot X_2 + 2.1(1 \pm 0.88) \cdot X_1 \cdot X_2 + 6.05(1 \pm 0.31) \cdot X_1^2 \quad (5)$$

$$Y_5 = 13.34(1 \pm 0.051) + 0.496(1 \pm 1.29) \cdot X_1 + 1.36(1 \pm 0.47) \cdot X_2 - 1.07(1 \pm 0.85) \cdot X_1 \cdot X_2 - 6.5(1 \pm 0.144) \cdot X_1^2 \quad (6)$$

$$Y_6 = 77.41(1 \pm 0.019) + 9.88(1 \pm 0.094) \cdot X_1 + 5.68(1 \pm 0.163) \cdot X_2 + 0.205(1 \pm 4.52) \cdot X_3 - 5.21(1 \pm 0.262) \cdot X_1^2 - 1.35(1 \pm 1.01) \cdot X_2^2 - 2.12(1 \pm 0.641) \cdot X_3^2 \quad (7)$$

Table 5. ANOVA statistical parameters evidencing the adequacy of the models.

Model	Dependent Variable	Determination Coefficient, R ²	Adjusted R ²	Calculated F-Value	p-Value
Model 1	Y_1	0.9793	0.9678	85.08	0.001
Model 2	Y_2	0.9803	0.9656	64.49	0.001
Model 3	Y_3	0.9788	0.9630	61.65	0.001
Model 4	Y_4	0.9189	0.8865	28.33	0.001
Model 5	Y_5	0.9639	0.9494	66.72	0.001
Model 6	Y_6	0.9911	0.9844	148.39	0.001

The main, binary, and quadratic interactions between the process factors can be evaluated based on the estimated coefficients and their confidence intervals in Relations (2)–(7). The statistical significance of the coefficients was evaluated through the p -value for each coefficient, and the ones that did not undergo proper significance were eliminated. Even so, few of the non-significant coefficients have been preserved in order to keep the hierarchy of the model (as they are involved in the binary/quadratic interactions).

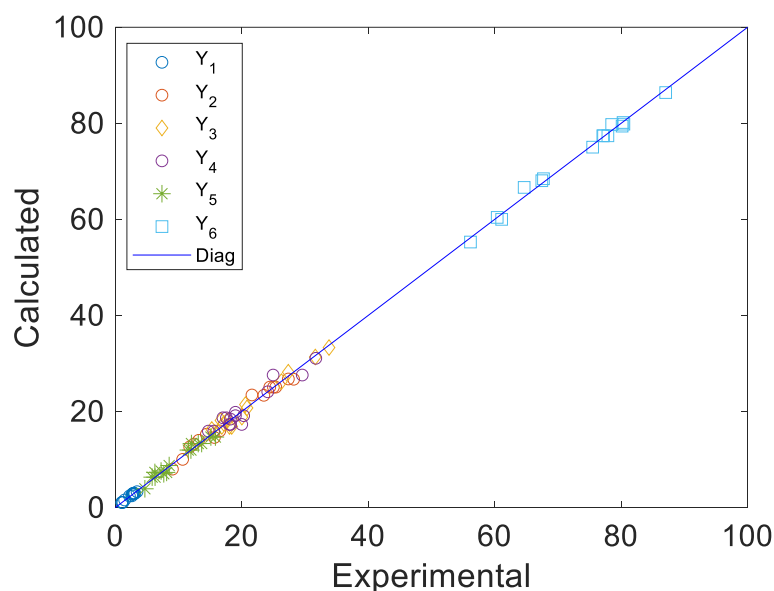
Based on preliminary experiments, the ranges for the main factors influencing the process were chosen between 80 and 120 °C for temperature, a catalyst amount between 1 and 5% (by weight), and an initial benzaldehyde to glycerol ratio between 1 and 1.2. The coded values of the factors corresponding to a Box–Behnken experimental design matrix together with the process responses are given in Table 4.

The experimental design matrix consists of 15 experiments, among which 3 are in the center of the experiment (experiments 7 to 9 in Table 4). The natural and coded independent variables together with their maximum and minimum limits are given in Table 6.

Table 6. Natural and coded values of the independent variables in the experimental design.

Factor	Value/Level					
	Low		Medium		High	
	Natural (Z)	Coded (X)	Natural (Z)	Coded (X)	Natural (Z)	Coded (X)
Temperature (°C), X_1	80	−1	100	0	120	+1
Catalyst amount (wt %), X_2	1	−1	3	0	5	+1
Initial B/Gly ratio (mol/mol), X_3	1	−1	1.1	0	1.2	+1

As mentioned in the experimental design literature [83], when working with coded variables, the magnitude of the coefficients gives an idea about the influence of the factor on the process response. Moreover, a positive coefficient means an increase in response to the factor, whereas a negative coefficient leads to a decrease in response to the increase of the factor. The models proposed in Relations (2)–(7) are rendered adequate, based on the correlation coefficients given in Table 5 (with values close to unity) and confirmed by the visual representation of the calculated vs. experimental data in the parity diagram in Figure 13. All these arguments prove a reasonably good representation of the process factors proposed by the mathematical models.

**Figure 13.** Parity diagram.

One aspect that must be emphasized is that the amount of benzoic acid obtained by hydrolysis of benzaldehyde in the reaction environment is relatively low. Figure 14 shows that the increase in temperature reduces the selectivity in benzoic acid (Y_1), a selectivity below 1% being obtained using a 5% catalyst and a B/Gly initial ratio of 1.2.

The values of the factors X_1 – X_3 in Table 7 have been obtained using the proposed mathematical models. The goal of this optimization study is the simultaneous maximization of glycerol conversion and selectivity in the 5-member and 6-member acetals (Y_2 , Y_3 , and Y_4), together with the simultaneous minimization of by-products (benzoic acid (Y_1) and non-cyclic acetals (Y_5)). The process factors ensuring the maximum values of glycerol conversion and selectivity in cyclic acetals are listed in Table 7.

A maximum glycerol conversion (85.95%) was obtained at 120 °C together with a 5% catalyst amount and a 1.15 molar ratio between glycerol and benzaldehyde. These parameters give a selectivity in cyclic acetals (Y_2 , Y_3 , and Y_4) of 78.56%.

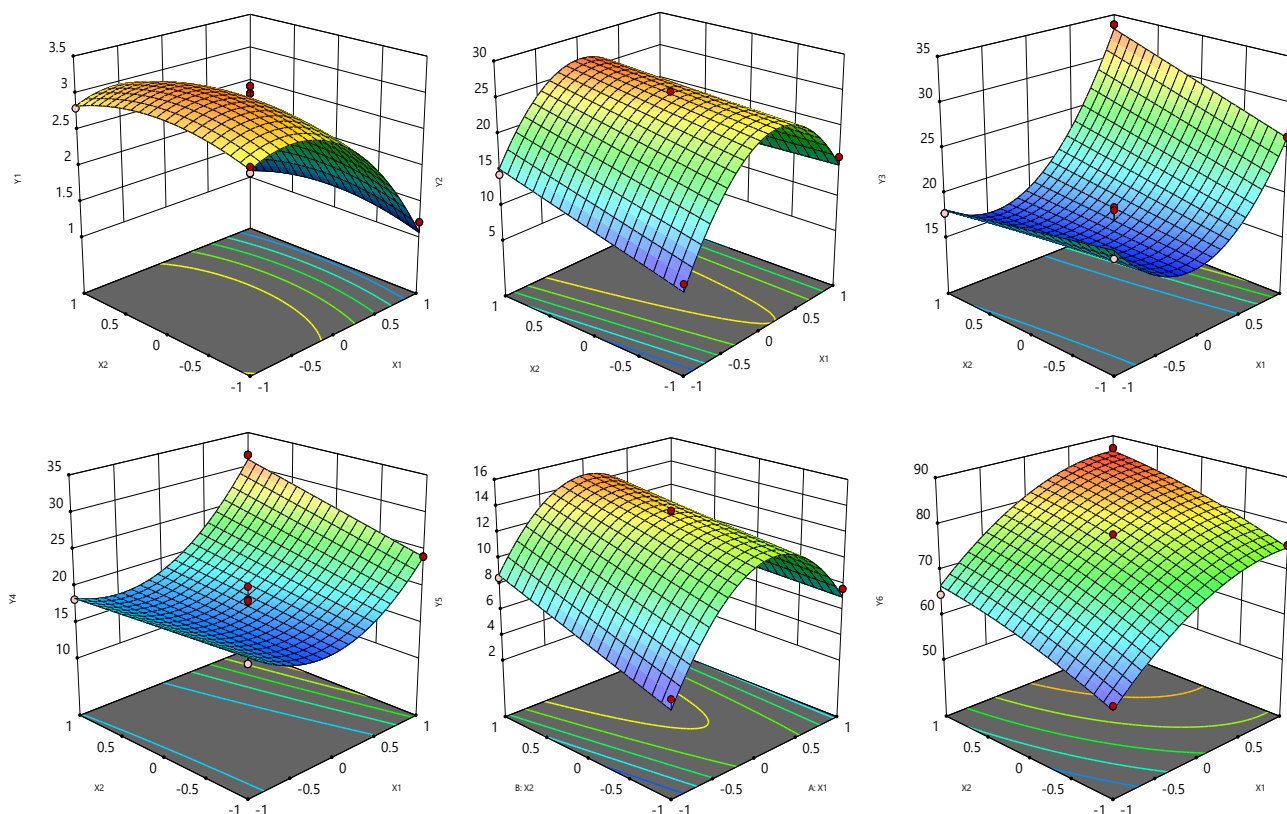


Figure 14. The response of the main variable to process factor variations.

Table 7. The optimized parameters for maximum values of glycerol conversion and selectivity in acetals.

X_1	X_2	X_3	Y_1	Y_2	Y_3	Y_4	Y_5	Y_6	Cycl
1	1	0.5	0.961	13.15	33.13	31.08	7.62	85.95	1
			1.11	12.46	32.85	30.12	6.38	82.91	2
1	1	0.5	1.23	12.25	31.85	29.87	6.08	81.31	3

In order to prove the reusability of the catalyst, three subsequent runs were carried out in the optimized conditions given in Table 7. These values show a slight decrease in glycerol conversion with no significant change in glycerol acetals. Similar results were reported by Yamamoto et al. [77] on a cationic acidic resin and by Samudrala et al. [84] over a mesoporous MCM-41 supported iron (III) chloride. The stability of the catalyst was proven by carrying out the FTIR analysis for pure, supported, and reused catalysts in the three cycles. The results are presented in Figure 15. The presence of immobilized HPW in the $\text{Fe}_3\text{O}_4@ \text{SiO}_2@ \text{HPW}$ catalyst after each cycle of utilization was proven mainly by the presence of the characteristic peaks of HPW at the 990 cm^{-1} (terminal bands for $\text{W}=\text{O}$ in the exterior WO_6 octahedron), 890 cm^{-1} , and 800 cm^{-1} (bands for the $\text{W}-\text{Ob}-\text{W}$ and $\text{W}-\text{Oc}-\text{W}$ bridge), suggesting that the keggel structure is still maintained. The peaks in the FTIR spectra corresponding to $1400\text{--}1600 \text{ cm}^{-1}$ are from the solvent used to wash the catalyst after each run.

The maximum value of glycerol conversion obtained in our study was about 86%, being among the highest values reported in the literature (Table 8), and the selectivity in cyclic acetals was also reasonably good.

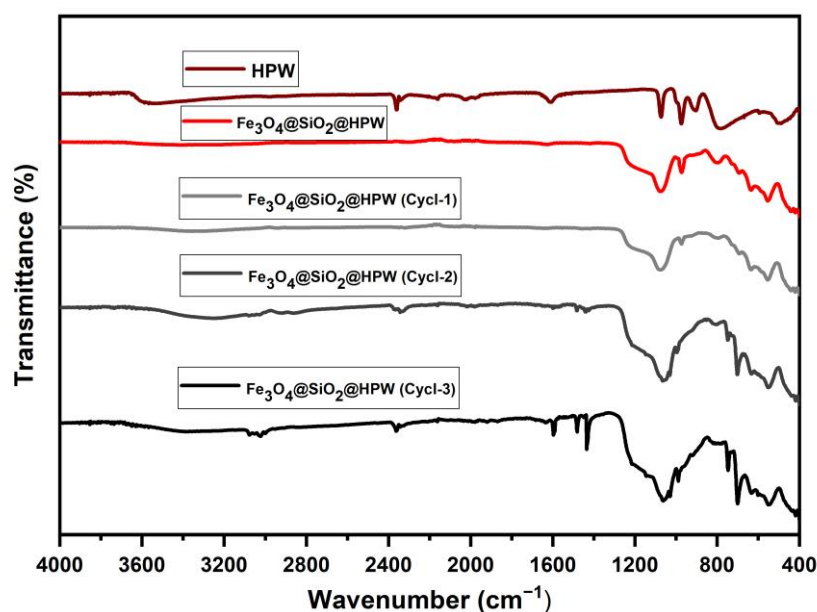


Figure 15. FTIR spectra of the HPW, supported HPW, and reused catalyst for three cycles.

Table 8. Acetalization of glycerol with benzaldehyde over other solid acid catalysts.

Catalyst	Reaction Conditions	Conversion/Yield (%)	Selectivity		Ref.
			Dioxolane	Dioxan	
p-toluenesulfonic acid	140 °C, 15 min, microwave (600 W), Gly/B = 1/1	67% (conv.)	47	53	[85]
20 % MoO ₃ /SiO ₂	100 °C, toluene as a solvent, 8 h, m _{cat} = 10 wt %, Gly/B = 1.1/1	72% (conv.)	40	60	[86]
MoO _x /TiO ₂ -ZrO ₂	100 °C, solventless, 30 min, m _{cat} = 5 wt %, Gly/B = 1/1	72% (conv.)	49	51	[87]
Amberlyst-36	61.2 °C, 0.1 MPa, refluxing chloroform as a solvent, 4 h, m _{cat} = 0.1 g, Gly/B = 1.1/1	94% (yield)	37	57	[88]
sulfonated graphene (GR-SO ₃ H)	100 °C, 14 h, m _{cat} = 25 mg, Gly/B = 1/10	92% (yield)	62	38	[89]
Ta/W (heteropoly acid)	25 °C, 1 h, 0.01 mmol (based on the Bronsted acid sites on the catalyst), Gly/B = 1/2	99% (conv.)	72	28	[90]

Given the activity of our catalyst, the synthesized Fe₃O₄@SiO₂@HPW catalyst was also tested in the acetalization of glycerol with other aromatic aldehydes: cinnamaldehyde and p-methyl-benzaldehyde, and the detected conversion of glycerol was 78% and 85%, respectively; the results are summarized in Table 9. However, in these conditions, the catalyst has a low activity for the acetalization of glycerol with vanillin and 4-hydroxybenzaldehyde (entries 3 and 4 in Table 9), which might be attributed to steric hindrance and mass transfer limitation. The selectivity in 5- and 6-member ring products for cinnamaldehyde and p-methyl-benzaldehyde is above 87%.

Table 9. Acetalization of glycerol with varied aromatic aldehydes on the catalyst.

Entry	Aldehyde	Conversion (%)	Selectivity	
			5-Member Ring	6-Member Ring
1	Cinnamaldehyde	78	57	30
2	p-methyl-benzaldehyde	85	59	32
3	p-hydroxy-benzaldehyde	-	-	-
4	vanillin	2	-	-

Reaction conditions: 100 °C, heptane as solvent, reaction time of 120 min, $m_{\text{cat}} = 5 \text{ wt}\%$, glycerol/aldehyde = 1/1.

3. Materials and Methods

3.1. Materials

$\text{FeCl}_3 \times 6\text{H}_2\text{O}$ (Carl Roth, Karlsruhe, Germany, min. 98%), $\text{FeCl}_2 \times 4\text{H}_2\text{O}$ (VWR Chemicals, Vienna, Austria, min. 99%), TEOS (tetraethyl orthosilicate) -VWR Chemicals, GPR Reactpur, NH_4OH 25% (Chimreactiv, Bucharest, Romania), Glycerol 99% extra pure (Merck KGaA, Darmstadt, Germany), Benzaldehyde 98%+ (Merck KGaA), Ethanol 96% (Chimreactiv), and Tungstophosphoric acid hydrate (Merck KGaA).

3.2. Catalyst Preparation

Preparation of magnetite nanoparticles (Fe_3O_4): The magnetite nanoparticles (Fe_3O_4) were synthesized by chemical co-precipitation of chloride salts of Fe^{3+} and Fe^{2+} (in a 2:1 molar ratio) [91–93]. Specifically, 27.033 g of $\text{FeCl}_3 \cdot 6\text{H}_2\text{O}$ and 9.94 g of $\text{FeCl}_2 \cdot 4\text{H}_2\text{O}$ were dissolved in 350 mL of distilled water. The solution was stirred at room temperature, and 35 mL of ammonia solution (25 wt%) was added dropwise quickly. The black nanoparticles immediately precipitated, and the agitation of the mixture continued for 30 min. After completion of the reaction, the black nanoparticles were separated from the reaction system with a magnet and washed with distilled water until a negative chloride reaction (tested with AgNO_3) was produced. Finally, the obtained black nanoparticles of Fe_3O_4 were washed with ethanol and dried at 100 °C.

Synthesis of silica-coated magnetite nanoparticles ($\text{Fe}_3\text{O}_4@\text{SiO}_2$): Nanoparticles of Fe_3O_4 were coated with silica using the modified Stöber method [94], which implies adding the Fe_3O_4 nanoparticles into a TEOS solution. First, the TEOS solution was prepared by adding 10 mL TEOS into a 200 mL mixture of ethanol-water (3:1 vol%), and the pH was fixed between 11 and 12 with an ammonia solution (25%). After approximately 20 min of mixing, when the solution started to become cloudy, 4 g of Fe_3O_4 nanoparticles were added to the solution, and the stirring continued for 4 h. All steps were performed at room temperature. The produced brown-grey sediment was separated from the solution with a magnet, washed with ethanol, and dried at 100 °C in air.

Immobilization of HPW: The HPW was immobilized onto the $\text{Fe}_3\text{O}_4@\text{SiO}_2$ using the impregnation method. To a solution of 5 g of $\text{Fe}_3\text{O}_4@\text{SiO}_2$ particles well dispersed in 50 mL of ethanol was added 1 g of HPW, and the mixture was continuously stirred for 24 h at room temperature. The resultant $\text{Fe}_3\text{O}_4@\text{SiO}_2@\text{HPW}$ particles were dried at 100 °C and calcinated at 300 °C for 3 h (heating rate of 10 °C/min). The calcination temperature was selected based on the thermal stability of the HPW to preserve the HPW Keggin structure [95].

3.3. Catalyst Characterization

The catalyst was characterized using different analytical methods: FTIR spectroscopy, SEM and XRD analyses, acidity evaluation, N_2 adsorption/desorption, and thermogravimetric analysis. Meanwhile, FTIR spectroscopy, acidity evaluation, and thermal analysis were employed for the spent catalyst to confirm its stability.

FTIR spectroscopy was performed on an IR Tracer-100 (Shimadzu Europa GmbH) Shimadzu Fourier-Transform Infrared Spectrophotometer using the KBr pellet technique, and the scanning wavelength range was 4000–400 cm^{-1} . The acidic properties of the catalyst (the concentrations of Brønsted and Lewis acid sites) were evaluated through the FTIR analysis of pyridine adsorption by the ring vibration of pyridine detected in the frequency range of 1400–1600 cm^{-1} .

The XRD measurements were run at room temperature using a Shimadzu 6000 XRD diffractometer (Shimadzu Corporation, Kyoto, Japan) with a monochromator of graphite for the $\text{Cu-K}\alpha$ radiation. The source power was operated at a voltage of 40 kV, an electrical current of 30 mA, and the scan speed was 2°/min. The PDF2 reference library was used for qualitative identification of the crystalline phases.

The surface area, pore volume, and pore size were measured by nitrogen adsorption-desorption isotherms at 77 K using a Micromeritics Tri Star II 3020 instrument (Unterschleissheim, Germany). Firstly, the sample was decontaminated under nitrogen flow at 100 °C for 24 h. The surface area was determined using the BET (Brunauer–Emmett–Teller) method. The micropore area and volume were obtained by applying the t-plot method. For the determination of meso- and macro-pore area and volume, we applied the BJH method on the isotherm desorption branch.

Thermogravimetric analyses (TGA) of the catalyst were recorded on a TGA/-IST (Thermal Analysis System TGA 2, METTLER TOLEDO, Greifensee, Switzerland) in the 25–600 °C temperature range, in a nitrogen atmosphere, with a heating rate of 10 °C/min.

External surface, morphology, and structure of catalysts were visualized by Scanning Electron Microscopy (SEM) using a QUANTA 133 Electron Microscope (FEI Company, Hillsboro, OR, USA) and a transmission electron microscopy (TEM) device coupled with an EDX detector (FEI Tecnai F20G2 TWIN Crio-TEM and X-MaxN 80T detector).

3.4. Catalyst Testing Procedure

A typical acetalization of glycerol with benzaldehyde was carried out in a 50 mL stirred three-neck flat-bottom flask, connected to a condenser in order to condense and reflux all the vapors keeping the reaction volume approximately constant. The reaction temperature was controlled by an external thermostat containing a thermocouple placed inside the reacting mixture. In a typical experiment, the flask was first charged with 0.1 moles glycerol, 0.1 moles benzaldehyde, 10 mL of solvent (hexane, heptane, or toluene), 0.46 g catalyst, and heated to the desired temperature. After the expected reaction time, the flask was cooled down to room temperature, and the solid catalyst was separated from the reaction mixture with a magnet, washed with distilled water and ethanol, and then kept for future recycling use.

The azeotropic distillation used in the esterification reaction leading to water elimination by creating an azeotrope mixture with an appropriate solvent is a technique widely used in the literature [23]. This was the reason for using different solvents in our experiments.

The reaction system formed biphasic layers (if toluene was used as solvent) or triphasic layers (if hexane/heptane was the used solvent). Owing to the self-separation characteristics, the upper/middle organic liquid layer containing products and reactant (mainly aldehyde) was easy to separate from the unreacted glycerol (the bottom layer).

The products from the reaction mixture were analyzed with a GC/MS 7000 Triple Quad MS (Agilent Technologies, Santa Clara, CA, USA) system equipped with an HP-FFAP (30 m, 250 mm, 0.25 mm) column and He as the carrier gas, with a volumetric flow of 1 mL/min.

3.5. Evaluation of Catalyst Performance Using Experimental Design Techniques

The performance of the acetalization of glycerol with benzaldehyde over the ferromagnetic catalyst was evaluated using a Box–Behnken experimental design, where 3 factors (independent variables) were considered: reaction temperature (X_1), catalyst amount (X_2), and the molar ratio between benzaldehyde and glycerol in the initial mixture (X_3). The reaction time considered for this evaluation was 120 min. The responses were glycerol conversion (Y_6) and the selectivity in the main reaction products: benzoic acid (Y_1), 2-phenyl-1,3-dioxolan-4-yl)methanol (Y_2), 2-Phenyl-1,3-dioxan-5-ol (Y_3) 2-phenyl-1,3-dioxolane (Y_4) and methyl 2-hydroxy-3-phenylpropanoate (Y_5).

4. Conclusions

In this study, a ferromagnetic heteropolyacid catalyst was successfully synthesized by immobilization of tungstophosphoric acid ($H_3PW_{12}O_{40}$; HPW) on a silica-coated magnetite, obtained by co-precipitation method. The characteristics of the catalyst were proven through SEM-EDX, XRD, and FT-IR analysis, which present the chemical and structural information. The EDS showed a good distribution of the active species on the catalyst surface, whereas TEM analysis showed an HPW particle size of 50 nm. The concentra-

tion of Brønsted and Lewis acid sites in the catalyst was 63.28 mmol/g, and the specific surface area was 40.86 m²/g. The so-prepared catalyst possesses not only easy separation property due to the magnetic core but also a superior catalytic activity for glycerol acetalization with benzaldehyde, with a maximum glycerol conversion of 96.1% and a cumulated acetal selectivity of about 78.36 %, in the optimized conditions (T = 120 °C, 5% wt catalyst and 1.15 glycerol/benzaldehyde molar ratio). The reuse in three subsequent runs proved the stability of the catalyst, with a slight decrease in glycerol concentration and no significant change in the acetals selectivities. The catalyst also exhibits excellent activity for glycerol acetalization with other aromatic aldehydes, such as cinnamaldehyde, p-methyl-benzaldehyde, p-hydroxy-benzaldehyde, and vanillin.

Supplementary Materials: The following supporting information can be downloaded at: <https://www.mdpi.com/article/10.3390/catal13040782/s1>, Figure S1. The GC-MS spectrum of a typical reaction mixture; Figure S2. The GC-MS signals of benzaldehyde; Figure S3. The GC-MS signals of benzoic acid; Figure S4. The GC-MS signals of 2-phenyl-1,3-dioxolan-4-yl) methanol; Figure S5. The GC-MS signals of 2-Phenyl-1,3-dioxan-5-ol; Figure S6. The GC-MS signals of 2-phenyl-1,3-dioxolane; Figure S7. The GC-MS signals of methyl 2-hydroxy-3-phenylpropanoate

Author Contributions: R.D.: Experimental, mathematical modeling; A.T.: Conceptualization, experimental, wrote the draft of the manuscript; Catalyst characterization; E.M.: Conceptualization, wrote the draft of the manuscript; M.R.: Catalyst characterization; D.P.: Catalyst characterization; I.B.: Mathematical modeling, revised the final version; R.G.: Revised the final version. All authors have read and agreed to the published version of the manuscript.

Funding: This research was funded by the Ministry of Research, Innovation, and Digitization, CNCS/CCCDI—UEFISCDI, grant number PD67/2020, within PNCDI III.

Data Availability Statement: Not applicable.

Conflicts of Interest: The authors declare no conflict of interest. The authors declare that they have no known competing financial interests or personal relationships that could have appeared to influence the work reported in this paper.

References

1. Ma, T.; Yin, M.; Su, C.; Guo, N.; Huang, X.; Han, Z.; Wang, Y.; Chen, G.; Yun, Z. Recent developments in the field of dehydration of bio-renewable glycerol to acrolein over molecular sieve catalysts. *J. Ind. Eng. Chem.* **2023**, *117*, 85–102. [[CrossRef](#)]
2. Ma, T.; Ding, J.; Shao, R.; Xu, W.; Yun, Z. Dehydration of glycerol to acrolein over Wells–Dawson and Keggin type phosphotungstic acids supported on MCM-41 catalysts. *Chem. Eng. J.* **2017**, *316*, 797–806. [[CrossRef](#)]
3. Ding, J.; Ma, T.; Cui, M.; Shao, R.; Guan, R.; Wang, P. Gas phase dehydration of glycerol to acrolein over Cs_{2.5}H_{0.5}PW₁₂O₄₀/Zr-MCM-41 catalysts prepared by supercritical impregnation. *Mol. Catal.* **2018**, *461*, 1–9. [[CrossRef](#)]
4. Ramirez Caballero, G.E.; Ardila Suárez, C.; Rojas Cristancho, J.Z.; Pineda Martínez, J.P.; Ramírez García, A. Effect of impurities in the crude glycerol polymerization reaction to produce polyglycerol. *CTF-Cienc. Tecnol. Y Futuro* **2019**, *9*, 89–98. [[CrossRef](#)]
5. Ebadipour, N.; Paul, S.; Katryniok, B.; Dumeignil, F. Calcium Hydroxyapatite: A Highly Stable and Selective Solid Catalyst for Glycerol Polymerization. *Catalysts* **2021**, *11*, 1247. [[CrossRef](#)]
6. Caputo, D.; Casiello, M.; Milella, A.; Oberhauser, W.; Maffezzoli, A.; Nacci, A.; Fusco, C.; D’Accolti, L. Deep Control of Linear Oligomerization of Glycerol Using Lanthanum Catalyst on Mesoporous Silica Gel. *Catalysts* **2020**, *10*, 1170. [[CrossRef](#)]
7. Ebadipour, N.; Paul, S.; Katryniok, B.; Dumeignil, F. Alkaline-Based Catalysts for Glycerol Polymerization Reaction: A Review. *Catalysts* **2020**, *10*, 1021. [[CrossRef](#)]
8. Banu, I.; Bumbac, G.; Bombos, D.; Velea, S.; Gălan, A.-M.; Bozga, G. Glycerol acetylation with acetic acid over Purolite CT-275. Product yields and process kinetics. *Renew. Energ.* **2020**, *148*, 548–557. [[CrossRef](#)]
9. Britto, P.J.; Kulkarni, R.M.; Veluturla, S.; Narula, A. Application of Steapsin lipase for bioconversion of glycerol acetates from glycerol. *Biocatal. Agric. Biotechnol.* **2023**, *48*, 102641. [[CrossRef](#)]
10. Shafiei, A.; Rastegari, H.; Ghaziaskar, H.S.; Yalpani, M. Glycerol transesterification with ethyl acetate to synthesize acetins using ethyl acetate as reactant and entrainer. *Biofuel Res. J.* **2017**, *4*, 565–570. [[CrossRef](#)]
11. Omar, L.; Perret, N.; Daniele, S. Self-Assembled Hybrid ZnO Nanostructures as Supports for Copper-Based Catalysts in the Hydrogenolysis of Glycerol. *Catalysts* **2021**, *11*, 516. [[CrossRef](#)]
12. Luciani, G.; Ruoppolo, G.; Landi, G.; Gargiulo, V.; Alfè, M.; Di Benedetto, A. Glycerol Hydrogenolysis to 1,2-Propanediol over Novel Cu/ZrO₂ Catalysts. *Catalysts* **2022**, *12*, 72. [[CrossRef](#)]
13. Sun, P.; Zhang, W.; Yu, X.; Zhang, J.; Xu, N.; Zhang, Z.; Liu, M.; Zhang, D.; Zhang, G.; Liu, Z.; et al. Hydrogenolysis of Glycerol to Propylene Glycol: Energy, Tech-Economic, and Environmental Studies. *Front. Chem.* **2022**, *9*, 1010. [[CrossRef](#)] [[PubMed](#)]

14. Bumbac, G.; Banu, I. Modeling and simulation process for solketal synthesis from glycerol and acetone by catalytic distillation in a modified structure of a divided wall column. *Renew. Energy* **2022**, *183*, 662–675. [[CrossRef](#)]
15. Razali, N.; McGregor, J. Improving Product Yield in the Direct Carboxylation of Glycerol with CO₂ through the Tailored Selection of Dehydrating Agents. *Catalysts* **2021**, *11*, 138. [[CrossRef](#)]
16. Procopio, D.; Di Gioia, M.L. An Overview of the Latest Advances in the Catalytic Synthesis of Glycerol Carbonate. *Catalysts* **2022**, *12*, 50. [[CrossRef](#)]
17. Li, H.; Zhang, Y.; Fu, P.; Wei, R.; Li, Z.; Dai, L.; Zhang, A. Chemical looping steam reforming of glycerol for hydrogen production over NiO–Fe₂O₃/Al₂O₃ oxygen carriers. *RSC Adv.* **2022**, *12*, 24014–24025. [[CrossRef](#)]
18. Sad, M.E.; Duarte, H.A.; Vignatti, C.; Padró, C.L.; Apesteguía, C.R. Steam reforming of glycerol: Hydrogen production optimization. *Int. J. Hydrogen Energy* **2015**, *40*, 6097–6106. [[CrossRef](#)]
19. Fasolini, A.; Cespi, D.; Tabanelli, T.; Cucciniello, R.; Cavani, F. Hydrogen from Renewables: A Case Study of Glycerol Reforming. *Catalysts* **2019**, *9*, 722. [[CrossRef](#)]
20. Ishida, K.; Aida, T. Vanillin Acetals. US 8.236.970, 7 August 2012.
21. Castro, G.A.D.; Santos, A.L.Q.; Sathicq, Á.G.; Palermo, V.; Romanelli, G.P.; Fernandes, S.A. Sustainable synthesis of acetals from glycerol as potential additives for biofuels under solvent-free conditions. *React. Chem. Eng.* **2022**, *7*, 2132–2140. [[CrossRef](#)]
22. García, E.; Laca, M.; Pérez, E.; Garrido, A.; Peinado, J. New Class of Acetal Derived from Glycerin as a Biodiesel Fuel Component. *Energy Fuels* **2008**, *22*, 4274–4280. [[CrossRef](#)]
23. Smirnov, A.A.; Selishcheva, S.A.; Yakovlev, V.A. Acetalization Catalysts for Synthesis of Valuable Oxygenated Fuel Additives from Glycerol. *Catalysts* **2018**, *8*, 595. [[CrossRef](#)]
24. Oprescu, E.-E.; Stepan, E.; Dragomir, R.E.; Radu, A.; Rosca, P. Synthesis and testing of glycerol ketals as components for diesel fuel. *Fuel Process. Technol.* **2013**, *110*, 214–217. [[CrossRef](#)]
25. Nanda, M.R.; Zhang, Y.; Yuan, Z.; Qin, W.; Ghaziaskar, H.S.; Xu, C. Catalytic conversion of glycerol for sustainable production of solketal as a fuel additive: A review. *Renew. Sustain. Energy Rev.* **2016**, *56*, 1022–1031. [[CrossRef](#)]
26. Calvo-Flores, F.G.; Monteagudo-Arrebola, M.J.; Dobado, J.A.; Isac-García, J. Green and Bio-Based Solvents. *Top. Curr. Chem.* **2018**, *376*, 18. [[CrossRef](#)] [[PubMed](#)]
27. Bigorra Llosas, J.; Sato, S.; Bueno, R.; Graupera, E. Use of Glycerol Acetals. WO 2009/049840 A1, 15 August 2008.
28. Schuch, C.M.; Malheiro, A.; Rodrigues, J.L.; Lago, G. Ether-ester de cetal ou d'acetal de glycerol, procedes de preparation, utilisations et compositions le comprenant. WO 2016/097840 A1, 21 April 2016.
29. Kirchhecker, S.; Dell'Acqua, A.; Angenvoort, A.; Spannenberg, A.; Ito, K.; Tin, S.; Taden, A.; de Vries, J.G. HMF–glycerol acetals as additives for the debonding of polyurethane adhesives. *Green Chem.* **2021**, *23*, 957–965. [[CrossRef](#)]
30. Güemez, M.B.; Requies, J.; Agirre, I.; Arias, P.L.; Barrio, V.L.; Cambra, J.F. Acetalization reaction between glycerol and n-butylaldehyde using an acidic ion exchange resin. Kinetic modelling. *Chem. Eng. J.* **2013**, *228*, 300–307. [[CrossRef](#)]
31. Shirani, M.; Ghaziaskar, H.S.; Xu, C. Optimization of glycerol ketalization to produce solketal as biodiesel additive in a continuous reactor with subcritical acetone using PuroLite® PD206 as catalyst. *Fuel Process. Technol.* **2014**, *124*, 206–211. [[CrossRef](#)]
32. Kowalska-Kuś, J.; Held, A.; Nowińska, K. A continuous-flow process for the acetalization of crude glycerol with acetone on zeolite catalysts. *Chem. Eng. J.* **2020**, *401*, 126143. [[CrossRef](#)]
33. Vannucci, J.A.; Legnoverde, M.S.; Dalla Costa, B.O.; Basaldella, E.I.; Nichio, N.N.; Pompeo, F. Al-free Zr-beta zeolite as a selective catalyst for the ketalization of glycerol. *Mol. Catal.* **2022**, *528*, 112497. [[CrossRef](#)]
34. Serafim, H.; Fonseca, I.M.; Ramos, A.M.; Vital, J.; Castanheiro, J.E. Valorization of glycerol into fuel additives over zeolites as catalysts. *Chem. Eng. J.* **2011**, *178*, 291–296. [[CrossRef](#)]
35. Arias, K.S.; Garcia-Ortiz, A.; Climent, M.J.; Corma, A.; Iborra, S. Mutual Valorization of 5-Hydroxymethylfurfural and Glycerol into Valuable Diol Monomers with Solid Acid Catalysts. *ACS Sustain. Chem. Eng.* **2018**, *6*, 4239–4245. [[CrossRef](#)]
36. Khayoon, M.S.; Hameed, B.H. Solventless acetalization of glycerol with acetone to fuel oxygenates over Ni–Zr supported on mesoporous activated carbon catalyst. *Appl. Catal. A Gen.* **2013**, *464–465*, 191–199. [[CrossRef](#)]
37. Khayoon, M.S.; Abbas, A.; Hameed, B.H.; Triwahyono, S.; Jalil, A.A.; Harris, A.T.; Minett, A.I. Selective Acetalization of Glycerol with Acetone Over Nickel Nanoparticles Supported on Multi-Walled Carbon Nanotubes. *Catal. Lett.* **2014**, *144*, 1009–1015. [[CrossRef](#)]
38. Kapkowski, M.; Ambrozkiewicz, W.; Siudyga, T.; Sitko, R.; Szade, J.; Klimontko, J.; Balin, K.; Lelaćko, J.; Polanski, J. Nano silica and molybdenum supported Re, Rh, Ru or Ir nanoparticles for selective solvent-free glycerol conversion to cyclic acetals with propanone and butanone under mild conditions. *Appl. Catal. B Environ.* **2017**, *202*, 335–345. [[CrossRef](#)]
39. Hong, G.H.; Li, Z.; Park, J.S.; Li, Z.; Kim, K.Y.; Li, C.; Lee, J.; Jin, M.; Stucky, G.D.; Kim, J.M. Glycerol acetalization over highly ordered mesoporous molybdenum dioxide: Excellent catalytic performance, recyclability and water-tolerance. *J. Ind. Eng. Chem.* **2022**, *107*, 354–364. [[CrossRef](#)]
40. Castanheiro, J.E.; Vital, J.; Fonseca, I.M.; Ramos, A.M. Acetalization of glycerol with hexanal in the presence of SBA-15 with sulfonic acid groups. *Catal. Today* **2022**, *384–386*, 2–11. [[CrossRef](#)]
41. Chen, L.; Nohair, B.; Zhao, D.; Kaliaguine, S. Glycerol acetalization with formaldehyde using heteropolyacid salts supported on mesostructured silica. *Appl. Catal. A Gen.* **2018**, *549*, 207–215. [[CrossRef](#)]
42. Chen, L.; Nohair, B.; Zhao, D.; Kaliaguine, S. Highly Efficient Glycerol Acetalization over Supported Heteropoly Acid Catalysts. *ChemCatChem* **2018**, *10*, 1918–1925. [[CrossRef](#)]

43. Jiang, Y.; Zhou, R.; Ye, B.; Hou, Z. Acetalization of glycerol over sulfated UiO-66 under mild condition. *J. Ind. Eng. Chem.* **2022**, *110*, 357–366. [[CrossRef](#)]
44. Bakuru, V.R.; Churipard, S.R.; Maradur, S.P.; Kalidindi, S.B. Exploring the Brønsted acidity of UiO-66 (Zr, Ce, Hf) metal–organic frameworks for efficient solketal synthesis from glycerol acetalization. *Dalton Trans.* **2019**, *48*, 843–847. [[CrossRef](#)]
45. Bae, S.; Gim, S.; Kim, H.; Dorcet, V.; Pasturel, M.; Grenèche, J.-M.; Darbha, G.K.; Hanna, K. New Features and Uncovered Benefits of Polycrystalline Magnetite as Reusable Catalyst in Reductive Chemical Conversion. *J. Phys. Chem. C* **2017**, *121*, 25195–25205. [[CrossRef](#)]
46. Arteaga-Díaz, S.J.; Meramo-Hurtado, S.I.; León-Pulido, J.; Zuorro, A.; González-Delgado, A.D. Environmental Assessment of Large Scale Production of Magnetite (Fe₃O₄) Nanoparticles via Coprecipitation. *Appl. Sci.* **2019**, *9*, 1682. [[CrossRef](#)]
47. Tavares, M.G.; Duarte, J.L.d.S.; Oliveira, L.M.T.M.; Fonseca, E.J.S.; Tonholo, J.; Ribeiro, A.S.; Zanta, C.L.P.S. Reusable iron magnetic catalyst for organic pollutant removal by Adsorption, Fenton and Photo Fenton process. *J. Photochem. Photobiol. A Chem.* **2022**, *432*, 114089. [[CrossRef](#)]
48. Li, J.; You, J.; Wang, Z.; Zhao, Y.; Xu, J.; Li, X.; Zhang, H. Application of α -Fe₂O₃-based heterogeneous photo-Fenton catalyst in wastewater treatment: A review of recent advances. *J. Environ. Chem. Eng.* **2022**, *10*, 108329. [[CrossRef](#)]
49. Singh, H.; Ali, A. Potassium and 12-tungstophosphoric acid loaded alumina as heterogeneous catalyst for the esterification as well as transesterification of waste cooking oil in a single pot. *Asia-Pac. J. Chem. Eng.* **2021**, *16*, e2585. [[CrossRef](#)]
50. Pekmezci Karaman, B.; Oktar, N. Tungstophosphoric acid incorporated hierarchical HZSM-5 catalysts for direct synthesis of dimethyl ether. *Int. J. Hydrogen Energy* **2020**, *45*, 34793–34804. [[CrossRef](#)]
51. Ferreira, P.; Fonseca, I.M.; Ramos, A.M.; Vital, J.; Castanheiro, J.E. Valorisation of glycerol by condensation with acetone over silica-included heteropolyacids. *Appl. Catal. B Environ.* **2010**, *98*, 94–99. [[CrossRef](#)]
52. Chen, L.; Nohair, B.; Kaliaguine, S. Glycerol acetalization with formaldehyde using water-tolerant solid acids. *Appl. Catal. A Gen.* **2016**, *509*, 143–152. [[CrossRef](#)]
53. Li, F.H.; Li, C.J.; Tchen, J.Y.; Wang, K.W.; Zhang, H.J.; Wang, Y.B.; Han, X.X. A Green and Sustainable Approach for Acetalization of Benzaldehyde Using Tungstophosphoric Acid Loaded on Metal Oxide Catalysts. *J. Chem. Soc. Pak.* **2019**, *41*, 805–819.
54. Castanheiro, J.E.; Mourão, P.A.; Cansado, I.; Vital, J.; Fonseca, I.M.; Ramos, A.M. Valorisation of glycerol with cinnamaldehyde over phosphotungstic acid encapsulated on a NaY zeolite. *Chem. Eng. Process.-Process Intensif.* **2022**, *177*, 108993. [[CrossRef](#)]
55. Hosseini, M.-S.; Masteri-Farahani, M. Fabrication of new magnetite based sulfonic-phosphotungstic dual-acid catalyst for catalytic acetalization of benzaldehyde with ethylene glycol. *React. Kinet. Mech. Catal.* **2020**, *130*, 979–991. [[CrossRef](#)]
56. Rajkumari, K.; Changmai, B.; Meher, A.K.; Vanlalveni, C.; Sudarsanam, P.; Wheatley, A.E.H.; Rokhum, S.L. A reusable magnetic nanocatalyst for bio-fuel additives: The ultrasound-assisted synthesis of solketal. *Sustain. Energy Fuels* **2021**, *5*, 2362–2372. [[CrossRef](#)]
57. Ishii, M.; Nakahira, M.; Yamanaka, T. Infrared absorption spectra and cation distributions in (Mn, Fe)₃O₄. *Solid State Commun.* **1972**, *11*, 209–212. [[CrossRef](#)]
58. Cui, H.; Ren, W.; Lin, P.; Liu, Y. Structure control synthesis of iron oxide polymorph nanoparticles through an epoxide precipitation route. *J. Exp. Nanosci.* **2013**, *8*, 869–875. [[CrossRef](#)]
59. Liang, Y.; Lu, W. Gamma-irradiation synthesis of Fe₃O₄/rGO nanocomposites as lithium-ion battery anodes. *J. Mater. Sci. Mater. Electron.* **2020**, *31*, 17075–17083. [[CrossRef](#)]
60. Jin, X.; Zhang, K.; Sun, J.; Wang, J.; Dong, Z.; Li, R. Magnetite nanoparticles immobilized Salen Pd (II) as a green catalyst for Suzuki reaction. *Catal. Commun.* **2012**, *26*, 199–203. [[CrossRef](#)]
61. Zhang, P.; Liu, P.; Fan, M.; Jiang, P.; Haryono, A. High-performance magnetite nanoparticles catalyst for biodiesel production: Immobilization of 12-tungstophosphoric acid on SBA-15 works effectively. *Renew. Energy* **2021**, *175*, 244–252. [[CrossRef](#)]
62. Husain, H.; Hariyanto, B.; Sulthonul, M.; Klysubun, W.; Darminto, D.; Pratapa, S. Structure and magnetic properties of silica-coated magnetite-nanoparticle composites. *Mater. Res. Express* **2019**, *6*, 086117. [[CrossRef](#)]
63. Gallego-Villada, L.A.; Alarcón, E.A.; Palermo, V.; Vázquez, P.G.; Romanelli, G.P. Kinetics for the biodiesel production from lauric acid over Keggin heteropolyacid loaded in silica framework. *J. Ind. Eng. Chem.* **2020**, *92*, 109–119. [[CrossRef](#)]
64. Abdollahi-Alibeik, M.; Mohammadpoor-Baltork, I.; Zaghaghi, Z.; Yousefi, B.H. Efficient synthesis of 1,5-benzodiazepines catalyzed by silica supported 12-tungstophosphoric acid. *Catal. Commun.* **2008**, *9*, 2496–2502. [[CrossRef](#)]
65. Wang, Y.; Hu, K.; He, J.; Zhang, Y. Improving the size uniformity of dendritic fibrous nano-silica by a facile one-pot rotating hydrothermal approach. *RSC Adv.* **2019**, *9*, 24783–24790. [[CrossRef](#)] [[PubMed](#)]
66. Xiao, H.; Zhang, J.; Wang, P.; Zhang, Z.; Zhang, Q.; Xie, H.; Yang, G.; Han, Y.; Tan, Y. Mechanistic insight to acidity effects of Ga/HZSM-5 on its activity for propane aromatization. *RSC Adv.* **2015**, *5*, 92222–92233. [[CrossRef](#)]
67. Isernia, L.F. FTIR study of the relation, between extra-framework aluminum species and the adsorbed molecular water, and its effect on the acidity in ZSM-5 steamed zeolite. *Mater. Res.* **2013**, *16*, 792–802. [[CrossRef](#)]
68. Shi, D.; Sadat, M.E.; Dunn, A.W.; Mast, D.B. Photo-fluorescent and magnetic properties of iron oxide nanoparticles for biomedical applications. *Nanoscale* **2015**, *7*, 8209–8232. [[CrossRef](#)] [[PubMed](#)]
69. Predescu, A.M.; Vidu, R.; Predescu, A.; Matei, E.; Pantilimon, C.; Predescu, C. Synthesis and characterization of bimodal structured Cu-Fe₃O₄ nanocomposites. *Powder Technol.* **2019**, *342*, 938–953. [[CrossRef](#)]
70. Mokkarat, A.; Kruanetr, S.; Sakee, U. One-step continuous flow synthesis of aminopropyl silica-coated magnetite nanoparticles. *J. Saudi Chem. Soc.* **2022**, *26*, 101506. [[CrossRef](#)]

71. Liu, C.; Li, Y.; Duan, Q. Preparation of magnetic and thermal dual-responsive zinc-tetracarboxyl-phthalocyanine-g-Fe₃O₄@SiO₂@TiO₂-g-poly(*N*-isopropyl acrylamide) core-shell green photocatalyst. *Appl. Surf. Sci.* **2020**, *503*, 144111. [[CrossRef](#)]
72. Vasudevan, S.V.; Kong, X.; Cao, M.; Wang, M.; Mao, H.; Bu, Q. Microwave-assisted liquefaction of carbohydrates for 5-hydroxymethylfurfural using tungstophosphoric acid encapsulated dendritic fibrous mesoporous silica as a catalyst. *Sci. Total Environ.* **2021**, *760*, 143379. [[CrossRef](#)]
73. Chai, S.-H.; Wang, H.-P.; Liang, Y.; Xu, B.-Q. Sustainable production of acrolein: Gas-phase dehydration of glycerol over 12-tungstophosphoric acid supported on ZrO₂ and SiO₂. *Green Chem.* **2008**, *10*, 1087–1093. [[CrossRef](#)]
74. Dias, J.A.; Caliman, E.; Loureiro Dias, S.C. Effects of cesium ion exchange on acidity of 12-tungstophosphoric acid. *Microporous Mesoporous Mater.* **2004**, *76*, 221–232. [[CrossRef](#)]
75. Alcañiz-Monge, J.; Bakkali, B.E.; Trautwein, G.; Reinoso, S. Zirconia-supported tungstophosphoric heteropolyacid as heterogeneous acid catalyst for biodiesel production. *Appl. Catal. B Environ.* **2018**, *224*, 194–203. [[CrossRef](#)]
76. Sing, K.S.W.; Everett, D.H.; Haul, R.A.W.; Moscou, L.; Pierotti, R.A.; Rouquerol, J.; Siemieniewska, T. Reporting Physisorption Data for Gas Solid Systems with Special Reference to the Determination of Surface-Area and Porosity (Recommendations 1984). *Pure Appl. Chem.* **1985**, *57*, 603–619. [[CrossRef](#)]
77. Yamamoto, K.; Kiyari, A.M.; Bagio, J.C.; Rossi, K.A.B.; Delabio Berezuk, F.; Berezuk, M.E. Green cyclic acetals production by glycerol etherification reaction with benzaldehyde using cationic acidic resin. *Green Process. Synth.* **2019**, *8*, 183–190. [[CrossRef](#)]
78. Castanheiro, J. Acetalization of Glycerol with Citral over Heteropolyacids Immobilized on KIT-6. *Catalysts* **2022**, *12*, 81. [[CrossRef](#)]
79. Patel, A.; Pithadia, D. Low temperature synthesis of bio-fuel additives via valorisation of glycerol with benzaldehyde as well as furfural over a novel sustainable catalyst, 12-tungstosilicic acid anchored to ordered cubic nano-porous MCM-48. *Appl. Catal. A: Gen.* **2020**, *602*, 117729. [[CrossRef](#)]
80. Kulkarni, R.M.; Arvind, N. Acetalization of glycerol and benzaldehyde to synthesize biofuel additives using SO₄²⁻/CeO₂-ZrO₂ catalyst. *Heliyon* **2021**, *7*, e06018. [[CrossRef](#)]
81. Myers, R.H.; Montgomery, D.C.; Anderson-Cook, C. *Response Surface Methodology Process and Product Optimization Using Designed Experiments*, 4th ed.; John Wiley & Sons, Inc.: Hoboken, NJ, USA, 2016; p. 40, 825 Seiten.
82. Navidi, W. *Statistics for Engineers and Scientists*, 3rd. ed.; McGraw-Hill: New York, NY, USA, 2011; p. 908 S.
83. Lazic, Z.R. *Design of Experiments in Chemical Engineering: A Practical Guide*; Wiley-VCH: Weinheim, Germany, 2004; 610p.
84. Samudrala, S.P.; Kandasamy, S.; Bhattacharya, S. One-pot synthesis of bio-fuel additives from glycerol and benzyl alcohol: Mesoporous MCM-41 supported iron (III) chloride as a highly efficient tandem catalyst. *Renew. Energ.* **2020**, *156*, 883–892. [[CrossRef](#)]
85. Pawar, R.R.; Jadhav, S.V.; Bajaj, H.C. Microwave-assisted rapid valorization of glycerol towards acetals and ketals. *Chem. Eng. J.* **2014**, *235*, 61–66. [[CrossRef](#)]
86. Umbarkar, S.B.; Kotbagi, T.V.; Biradar, A.V.; Pasricha, R.; Chanale, J.; Dongare, M.K.; Mamede, A.-S.; Lancelot, C.; Payen, E. Acetalization of glycerol using mesoporous MoO₃/SiO₂ solid acid catalyst. *J. Mol. Catal. A Chem.* **2009**, *310*, 150–158. [[CrossRef](#)]
87. Sudarsanam, P.; Malleshm, B.; Prasad, A.N.; Reddy, P.S.; Reddy, B.M. Synthesis of bio-additive fuels from acetalization of glycerol with benzaldehyde over molybdenum promoted green solid acid catalysts. *Fuel Process. Technol.* **2013**, *106*, 539–545. [[CrossRef](#)]
88. Deutsch, J.; Martin, A.; Lieske, H. Investigations on heterogeneously catalysed condensations of glycerol to cyclic acetals. *J. Catal.* **2007**, *245*, 428–435. [[CrossRef](#)]
89. Oger, N.; Lin, Y.F.; Le Grogne, E.; Rataboul, F.; Felpin, F.-X. Graphene-promoted acetalisation of glycerol under acid-free conditions. *Green Chem.* **2016**, *18*, 1531–1537. [[CrossRef](#)]
90. Peng, Q.; Zhao, X.; Li, D.; Chen, M.; Wei, X.; Fang, J.; Cui, K.; Ma, Y.; Hou, Z. Synthesis of bio-additive fuels from glycerol acetalization over a heterogeneous Ta/W mixed addenda heteropolyacid catalyst. *Fuel Process. Technol.* **2021**, *214*, 106705. [[CrossRef](#)]
91. Mascolo, M.C.; Pei, Y.; Ring, T.A. Room Temperature Co-Precipitation Synthesis of Magnetite Nanoparticles in a Large pH Window with Different Bases. *Materials* **2013**, *6*, 5549–5567. [[CrossRef](#)] [[PubMed](#)]
92. LaGrow, A.P.; Besenhard, M.O.; Hodzic, A.; Sergides, A.; Bogart, L.K.; Gavriilidis, A.; Thanh, N.T.K. Unravelling the growth mechanism of the co-precipitation of iron oxide nanoparticles with the aid of synchrotron X-ray diffraction in solution. *Nanoscale* **2019**, *11*, 6620–6628. [[CrossRef](#)]
93. Peternele, W.S.; Monge Fuentes, V.; Fascineli, M.L.; Rodrigues da Silva, J.; Silva, R.C.; Lucci, C.M.; Bentes de Azevedo, R. Experimental Investigation of the Coprecipitation Method: An Approach to Obtain Magnetite and Maghemite Nanoparticles with Improved Properties. *J. Nanomater.* **2014**, *2014*, 682985. [[CrossRef](#)]
94. Stöber, W.; Fink, A.; Bohn, E. Controlled growth of monodisperse silica spheres in the micron size range. *J. Colloid Interface Sci.* **1968**, *26*, 62–69. [[CrossRef](#)]
95. Siqueira Mancilha Nogueira, J.; Alves Silva, J.P.; Mussatto, S.I.; Melo Carneiro, L. Synthesis and Application of Heterogeneous Catalysts Based on Heteropolyacids for 5-Hydroxymethylfurfural Production from Glucose. *Energies* **2020**, *13*, 55. [[CrossRef](#)]

Disclaimer/Publisher's Note: The statements, opinions and data contained in all publications are solely those of the individual author(s) and contributor(s) and not of MDPI and/or the editor(s). MDPI and/or the editor(s) disclaim responsibility for any injury to people or property resulting from any ideas, methods, instructions or products referred to in the content.